The Dissertation Committee for Anshuman Cherala Certifies that this is the approved version of the following Dissertation:

Nanoshape Imprint Lithography: Fabrication and Modeling

Committee:

S.V Sreenivasan, Supervisor

Li Shi

Kenneth Liechti

Dragan Djurdjanovic

Nanoshape Imprint Lithography: Fabrication and Modeling

by

Anshuman Cherala

Dissertation

Presented to the Faculty of the Graduate School of

The University of Texas at Austin

in Partial Fulfillment

of the Requirements

for the Degree of

Doctor of Philosophy

The University of Texas at Austin

May 2019

Dedication

I dedicate this work to the armed forces of India and the United States of America and in particular to my relatives who have served:

- My grandfather, Ordnance Officer Tilak Sivaramakrishnan (British Indian and later Indian Army, Ordnance), who served notably during World War II and in Kashmir (1948).
- Pilot Officer Raghava Rao Cherala (Royal Indian Air Force), who died fighting the Luftwaffe over British skies in 1941.
- Staff Officer-Grade 1 (equivalent to Lieutenant Colonel) Ramachandran Sivaramakrishnan, who served in the Engineer-in-chief's branch of the British Indian and later Indian Army headquarters.
- Captain Sivaraman Ramachandran, who served in the Army Ordnance Corps.
- Colonel Ramachandran Kameswara Kumar, who was commissioned to the Corp of Engineers and took part in vanguard operations supporting forward deployed troops during the 1965 and 1971 wars.

Acknowledgements

I would like to thank my research supervisor Prof. S.V Sreenivasan for his patience, optimism and expert guidance that have made this work possible. I want to acknowledge the support and contributions as well as sacrifices made by my wife Sandya, my sons Akash and Aryash, my parents and my in-laws. I thank my labmates from the HTPN Lab, especially Ms. Akhila Mallavarapu and Dr. Bailey Yin for their work on the ultracapacitor fabrication. The MRC and Nascent ERC staff, especially, Dr. Shrawan Singhal, Dr. Ovadia Abed, Dr. Larry Dunn and Dr. Marylene Palard have been incredibly supportive towards making progress on my research. This research would also not have been possible without the support of Canon Nanotechnologies, so I am grateful for all their assistance. I would like to recognize the help I have received from past and present colleagues: Dr. Jin Choi, Dr. Dwayne LaBrake, Dr. Mark Mellier-smith, Mr. Gary Doyle, Ms. Georgia Rich, Mr. John Graves, Mr. Jason Farmer, Mr. Michael Miller, Dr. Vikramjit Singh, Dr. Sean Ahn, Mr. Mario Meissl, Mr. Seth Bamesberger, Dr. Se-Hyuk Im, Dr. Nilabh Roy, Mr. Matt Kincaid and Mr. Mahadevan Ganapathisubramanian

Abstract

Nanoshape Imprint Lithography: Fabrication and Modeling

Anshuman Cherala, Ph.D.

The University of Texas at Austin, 2019

Supervisor: S. V. Sreenivasan

Complex nanoshaped structures[1] have been shown to enable emerging nanoscale applications in energy, electronics, photonics and medicine. Such nanoshaped fabrication at high throughput is well beyond the capabilities of advanced optical lithography. Even the highest resolution electron beam lithography processes (Gaussian beam tools with non-chemically amplified resists) can achieve only ~10nm resolution, but at very low throughputs. In this work, fabrication of precise diamond-like nanoshapes with ~3nm radius corners is demonstrated using nanoimprint lithography. An exemplary shaped silicon nanowire ultracapacitor device was fabricated with these nanoshaped structures, wherein the half pitch was 100nm. The device significantly exceeded standard nanowire capacitor performance (by 90%) due to relative increase in surface area per unit projected area, enabled by the nanoshape. In the process of further scaling these nanoshaped structures to 10nm half pitch and below, a new "shape retention" resolution limit is observed due to polymer relaxation in imprint resists, which cannot be predicted with a

[1] Nanoshape structures here are defined as shapes enabled by sharp corners with radius of curvature < 5nm.

linear elastic continuum model. An all-atom molecular dynamics model of the nanoshape structure is developed to study this shape retention phenomenon and accurately predict the polymer relaxation. The atomistic framework has been used as a modeling and design tool to extend the capability of imprint lithography to sub 10nm nanoshapes. This framework can propose process refinements that maximize shape retention, and design template assist features (design for nanoshape retention) to achieve targeted nanoshapes.

Table of Contents

List of Tables

List of Figures

Chapter 1: *Introduction*

The general field of interest for this research work is the fabrication and modeling of nanoscale[2] structures. Fabrication of nanoscale structures falls under the purview of nanolithography. The field of nanolithography is vast, with optical lithography being the de-facto standard for high volume production of integrated circuit (IC) devices in logic and memory. Electron beam lithography is the industry standard for higher resolution features (up to ~10nm, on Gaussian beam tools with non-chemically amplified resists), but at very low throughput and is mostly used to make masks for optical lithography, templates for nanoimprint lithography, and nanopatterns for research purposes. This study focuses on complex nanoshaped[3] structures like diamond, cross and star shapes at dimensions well beyond the capability of optical and electron beam lithography techniques being used in the industry today.

MOTIVATION FOR NANOSHAPE STUDY

Shaped nanostructures have been shown to enable emerging applications in varied fields such as energy storage [1], nanoscale photonics [2], plasmonic nanostructures [3], multi-bit magnetic memory [4], terabit per sq. in. magnetic recording [5], and bio-nanoparticles [6, 7]. These applications require high throughput patterning with complex shape control at the nanoscale. Shaped nanopatterns exhibit novel optical, mechanical and morphological properties that are exploited in various ways by these emerging fields. The next few sections describe the various uses of nanoshaped structures in different fields.

[2] Nanoscale here refers to structures with their largest dimension less than 100nm.
[3] Nanoshape structures here are defined as shapes enabled by sharp corners with radius of curvature < 5nm.

Energy Storage

On-chip Metal-oxide-semiconductor (MOS) ultra-capacitors on silicon are a good application for nanoshape imprinting as they are easily integrated with existing CMOS architecture lithography layers as compared to package-level electrolytic capacitors. The benefits of such on-chip capacitors include faster speeds and lower interconnect impedance.

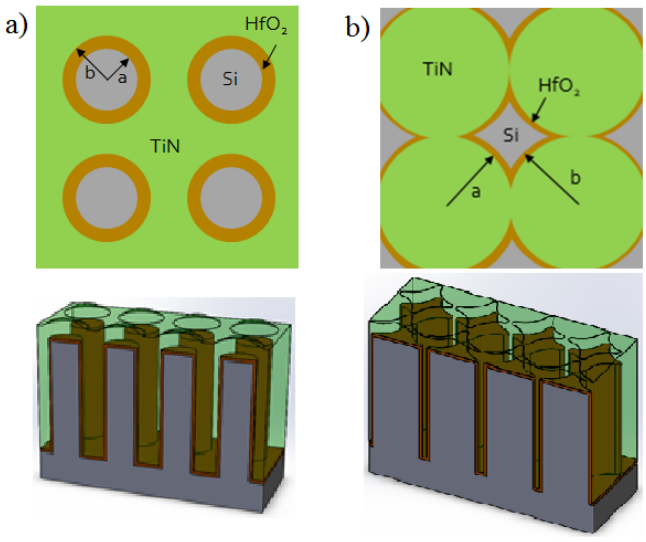

Figure 1: Top and 3D cross-sectional views of a) Circular cross section capacitor (left) and b) Diamond cross section capacitor (right); where *a* is the radius of the inner electrode and *b* is the radius of the outer electrode. The thin brown layer is the dielectric (HfO_2), the green bulk material is TiN and the grey wires and substrate are p-Si.

Although planar MOS capacitors can be implemented on chips, a prohibitively large chip area is required. With scalable, high aspect ratio nanoshape pillars, capacitors can be fabricated on the silicon chip providing the benefits of on-chip capacitors without area loss. Figure 1 shows schematic of circular and nanoshaped device structures. The nanoshaped device structures show ~90% increase in performance (details in Chapter 2).

Photonics

Inverse computational techniques to solve Maxwell's equations for photonics output complex nanoshapes as shown in Figure 2. As can be seen, these shapes have intricate topologies that need to be faithfully reproduced by any patterning technique to get the design performance.

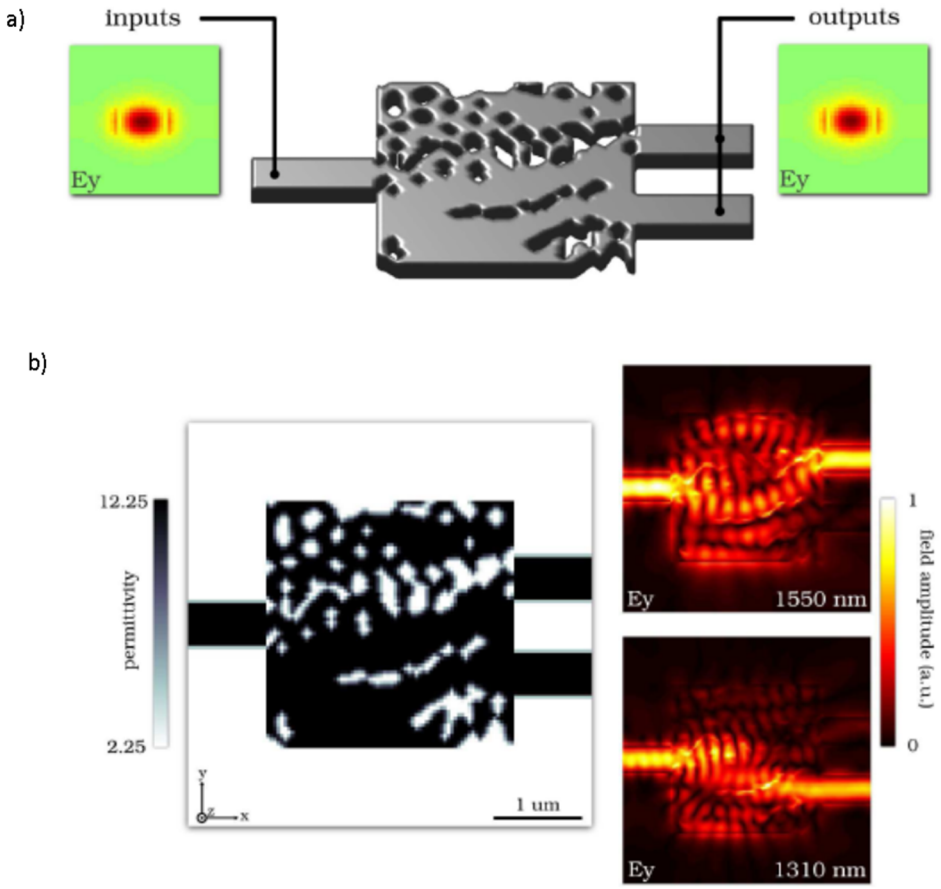

Figure 2: a) Wavelength splitter performance specification. Input mode is the fundamental TE polarized mode on the left at a wavelength of either 1550 nm or 1330 nm. Output modes are the fundamental waveguide modes of either output waveguide on the right; however, the 1550 nm wavelength is directed into the top output, while the 1310 nm wavelength is directed into the bottom output. Output power into the desired output arm is specified to be greater than 90%, while power into the opposing arm is set to below 1%.

b) Wavelength splitter final result. The conversion efficiencies into the upper and lower output arms are 83.2% and 78.7% respectively, while the rejection powers for the same modes are 0.49% and 1.66%. Device footprint is 2.8×2.8 microns. Source [2].

Plasmonic Structures

Classical bow-tie shaped plasmonic structures have been further fractalized to increase the resonance wavelengths and create efficient Surface-enhanced Raman spectroscopy substrates, while miniaturizing the features size as shown in Figure 3.

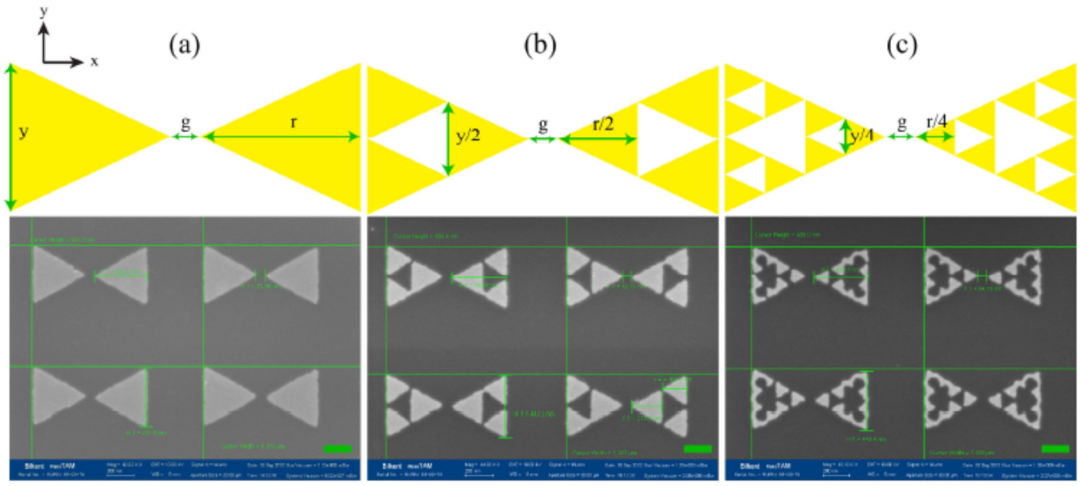

Figure 3: Schematics (above) and SEM (below) images of a) Bowtie, b) Fractal-1, and c) Fractal-2 structures. g = 65 nm, r = 400 nm, y = 420 nm. Scale bar is 100 nm. Source [3].

Multi-bit magnetic memory

Cross-shaped memory cells have been shown to enable multi-bit magnetic memory storage using spin transfer torque technology. The storage of multi-bits increases memory density of the device. Exemplary dimension of cross is shown in Figure 4.

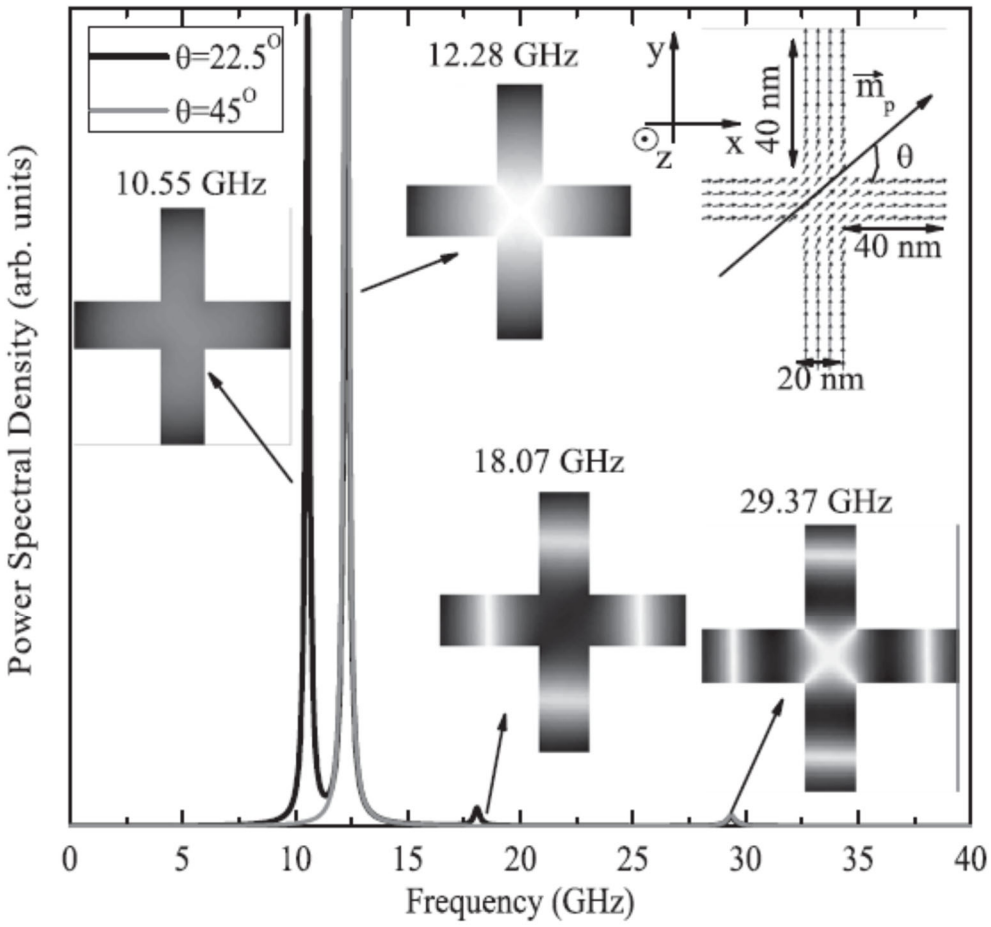

Figure 4: 2-bit STT-RAM cross shaped device. Power spectra of z-component of spatially varying magnetization of a symmetric cross for symmetric and asymmetric SPC. Spatial distribution of oscillation power corresponding to each peak is also shown (white to black represents lowest to highest power). The inset (top-right) shows cross dimensions and the direction of polarization of SPC (~mp) at an angle of θ, with the horizontal branch. Source [4].

Terabit per square inch magnetic recording

Shaped plasmonic structures have been used to locally heat a recording medium for increasing memory density in magnetic data storage. Figures 5d and 6a show the antenna shape required for this application.

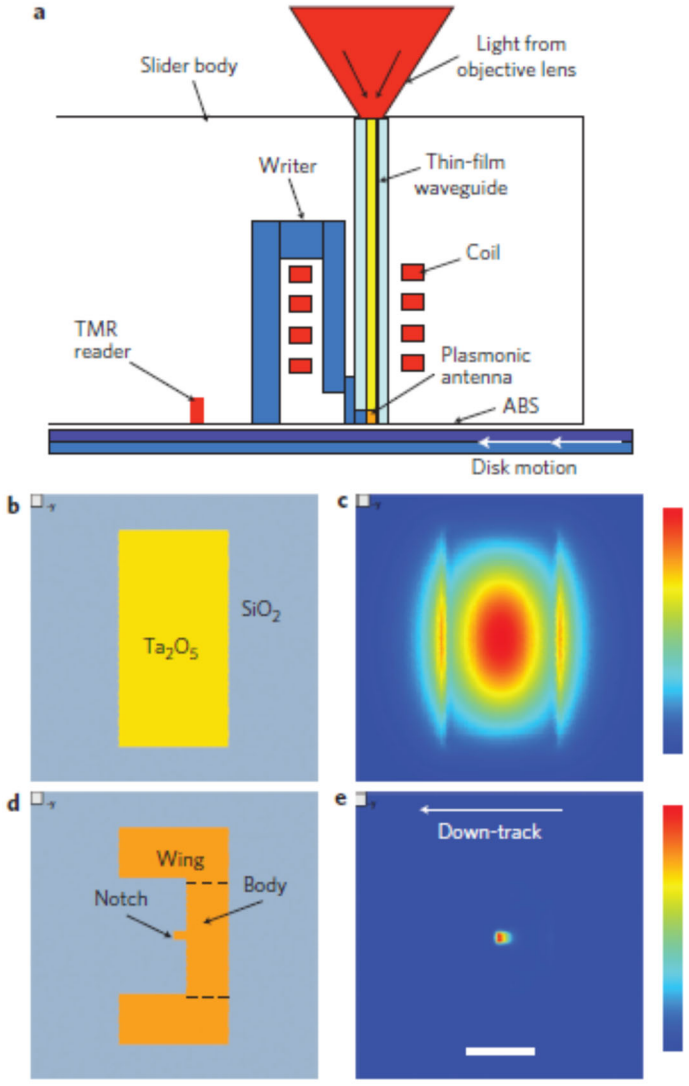

Figure 5: Bit patterned media: Integrated recording head schematic and modelling. a) Schematic showing the TAR head concept, including light delivery, waveguide, plasmonic antenna, magnetic writer, TMR reader and disk motion direction. b) Cross-section of waveguide with 600 nm× 300 nm Ta2O5 waveguide core. c) Modelled optical intensity in the waveguide at a laser wavelength of 830 nm, with SiO_2 cladding. The polarization is in the short-axis direction. The FWHM is approximately 400 nm× 250 nm. d) Cross-section of the E-antenna at the end of the waveguide (pole not included). The body dimensions are 316 nm× 114 nm, wing dimensions are 142 nm× 300 nm, and the notch dimensions are 24 nm (width)× 36 nm (length). The tip of the notch is below the center of the core. e) Finite-element modelled absorption profile at the disk surface below the E-antenna. The smallest element size used was a 1-nm cube. The in-page height of the gold is 98 nm, and the antenna is assumed to be separated from a 50-nm-thick cobalt medium by a 6-nm air gap. Scale bar, 200 nm (b–e). Source [5].

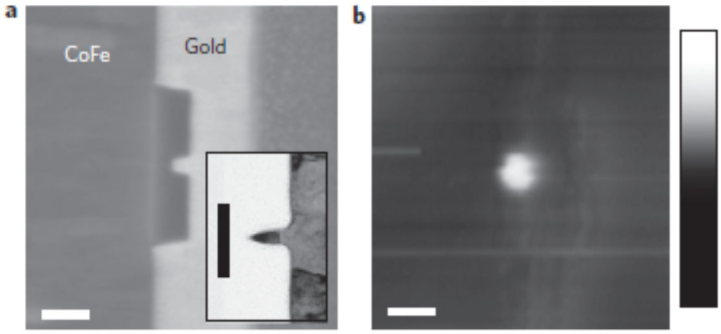

Figure 6: Fabricated plasmonic antenna and thermal probe imaging. a) SEM image of the E-antenna with integrated magnetic pole at the airbearing surface. The dielectric between the pole and antenna is SiO_2. Scale bar, 100 nm. Inset: TEM image of the E-antenna with a 10-nm-wide notch. Scale bar, 50 nm. b) Scanning thermal microscopy image of head output using a palladium thermistor wire tip at 10 nm lift height. Scale bar, 100 nm. Source [5].

Bio-nanoparticles

Nanoparticle shape has been shown to influence uptake in mammalian cells. Nanodiscs are preferred over nanorods as shown in Figure 7. This study of nanoparticle shape behavior is critical for improving the design of nanocarriers for targeted drug delivery.

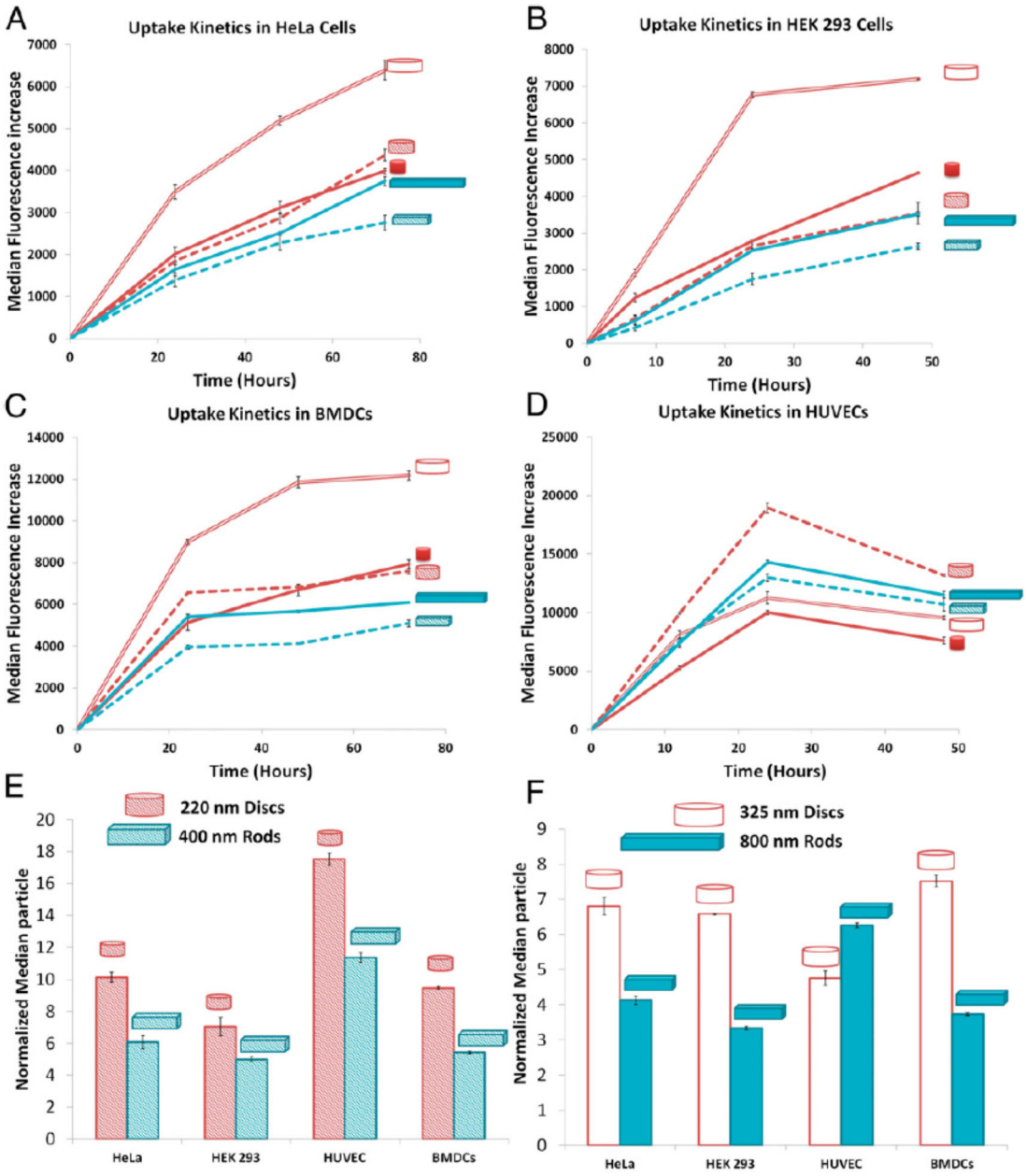

Figure 7: Cellular-uptake kinetics of different shape-specific nanoparticles in various cell lines. (A) HeLa cells, (B) HEK 293 cells, (C) BMDCs, and (D) HUVEC cells. In A–D, red lines are for nanodiscs (hollow for 325 × 100-nm discs, dashed for 220 × 100-nm discs, and solid for 80 × 70-nm discs), and blue lines are for nanorods (dashed for 400 × 100 × 100-nm rods and solid for 800 × 100 × 100-nm rods). Error bars are SD with n = 3 for each data point. (E–F) Normalized median particle uptake per cell (indicates relative number of particles internalized by cells when normalized to 100 particles of 80 × 70-nm discs) at the maximum internalization time point (72 h for HeLa and BMDC, 48 h for HEKs, and 24 h for endothelial cells).. Source [6].

NANOLITHOGRAPHY: STATE OF THE ART

Various lithography technologies have been developed over the years but optical lithography has become the industry standard over the last 50 years for high volume production of ICs. An increasing number of consumer products from cellphones to cars have logic and memory chips embedded in them. Every computer chip made over this time period was made with some form of optical lithography. There has been a race to miniaturize these IC devices since the early days of optical lithography to pack as many MOSFET transistors (the building block for most of these devices) as possible within the chip. The scaling of this miniaturization is captured in what is called Moore's Law (proposed by Gordon Moore, one of the co-founders of Intel Corp, a leading provider of ICs). Moore's Law states that the number of transistors per unit area roughly doubles every 18 months and this is formalized in the form of a roadmap by the International Technology Roadmap for Semiconductors (ITRS).

Photolithography

Photolithography uses photons of a single wavelength to transfer a circuit pattern from a mask onto a semiconductor wafer. The concept is shown schematically in Figure 8. The optical resolution limit, which is a metric for the smallest feature size that can resolved is given by $R = k*\lambda*/NA$ [9]. Where λ is the wavelength used, NA is the numerical aperture. k is a process dependent parameter. In an effort to keep up with Moore's Law, various technologies like x-ray, SCALPEL, 157nm photolithography have been tried and developed over the years. The current state-of-the-art photolithography tools (called *scanners* in industry parlance), use a 193nm wavelength excimer laser from an Argon-Fluoride source (ArF), with the wafer developed (a light sensitive film called photoresist is coated on the surface of the wafer) under a thin film of water (immersion lithography).

The water film, due to its larger refractive index compared to air, allows for finer resolution patterns to be transferred onto the wafer.

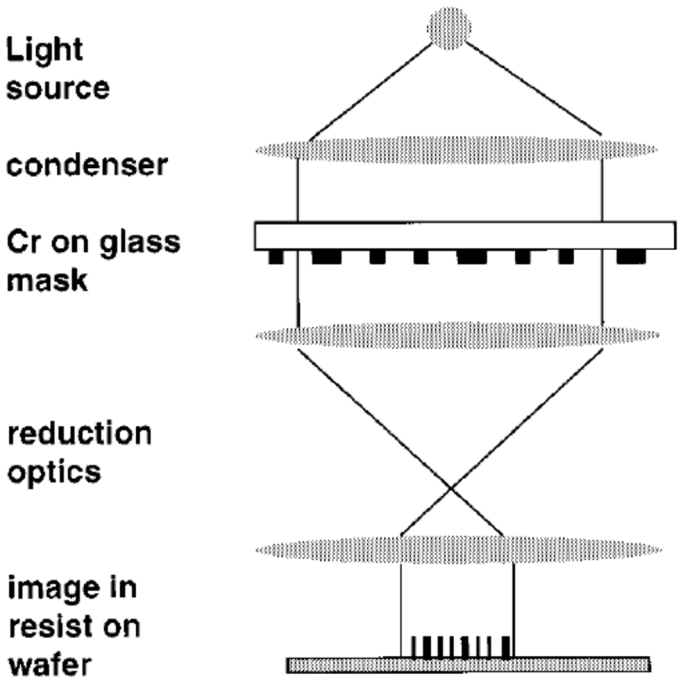

Figure 8: Schematic diagram of optical step-and-repeat lithography tool. Pattern on the mask usually represents one level of one (or sometimes a few) chip. Mask pattern is printed onto the wafer, then the wafer is moved to a new location, and the process is repeated until the entire wafer is exposed. Actual projection optical systems have 25 or more lens elements for aberration compensation and field flattening to achieve diffraction-limited performance. Source [8].

The limit of this state-of-the-art pattern transfer technique is about 38nm half-pitch for lines and spaces (gratings) and ~50nm half-pitch for more complex structures. Devices today already require tighter pitch to keep up with the ITRS road map. These devices are made by techniques like self-aligned double patterning (SADP) where by a deposition and etch step reduces the pitch of the gratings by half [10], self-aligned quad patterning (SADP done twice) and multiple lithography-etch steps where by a first layer is etched isotropically to reduce the feature size and a second layer is printed in the gaps created by

the first etch followed by a second etch step. These methods increase the cost of lithography and even then work only for regular patterns like gratings, posing severe constraints on device designs.

Imprint lithography

Imprint lithography has demonstrated large area patterning at sub-10 nm half-pitch with the capability to pattern typical lithographic structures such as lines, gratings, dot arrays etc. [11-14]. Due to its near molecular level of resolution over large areas and its progress in scalability, a particular form of imprint lithography called Jet and Flash Imprint Lithography (J-FIL) is a viable candidate for manufacturing sub-20 nm patterns in semiconductor devices [15] and for sub-10 nm patterns in hard disks [16]. In J-FIL, a low viscosity resist is deposited onto the substrate using an inkjet dispenser. This dispensing technique has been chosen in J-FIL to match the distribution of resist to the pattern density variation in the template, which enables high throughput patterning of arbitrary structures. The patterned template is then lowered onto the dispensed material on the substrate so that the relief patterns are filled by capillary action. The resist material which is an acrylate based multi-component formulation, is then cross-linked under UV radiation. Finally, the template is removed leaving a patterned resist on the substrate (Figure 9).

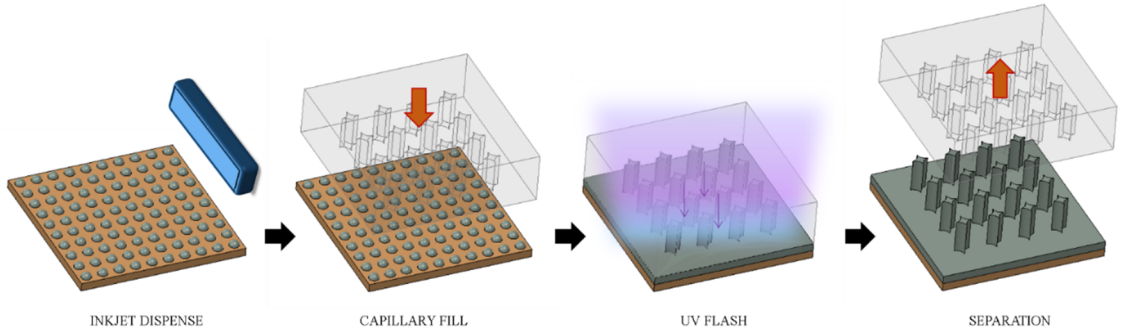

Figure 9: Jet and Flash Imprint Lithography.

Other lithography technologies

Other techniques that are being currently pursued or have been in use are surveyed briefly here.

Extreme Ultraviolet Lithography (EUV)

EUV uses soft x-rays of 13.2nm wavelength to create enhanced resolution beyond immersion lithography. While this technique appears to be a natural extension of photolithography, there are several challenges. The entire EUV photon path needs to be in vacuum since the wavelength is strongly absorbed by almost all materials. The optics are therefore reflective instead of transmittive, including the photomask. Source power, thermal management challenges and contamination issues have plagued the development this technology. However, along with J-FIL, EUV is the only other technology being seriously pursued to replace and complement optical immersion lithography [17].

Electron beam (e-beam) Lithography

E-beam lithography currently is used mostly to write the photomask and imprint masks. The highest resolution e-beam processes (Gaussian beam tools with non-chemically amplified resists) possesses resolution of ~10nm but at very low throughputs and thus exclude from high volume production. Multiple e-beam (MEBL) tools are in development to increase the process throughput [18, 19].

Directed Self Assembly Lithography (DSA)

Directed self-assembly uses the ability of block copolymers to preferentially assemble into periodic structures as shown in Figure 10 [20]. The technique is being

explore to complement photo lithography. DSA methods are suited for periodic patterns and also suffer from challenges in image placement of patterns and defects [21, 22].

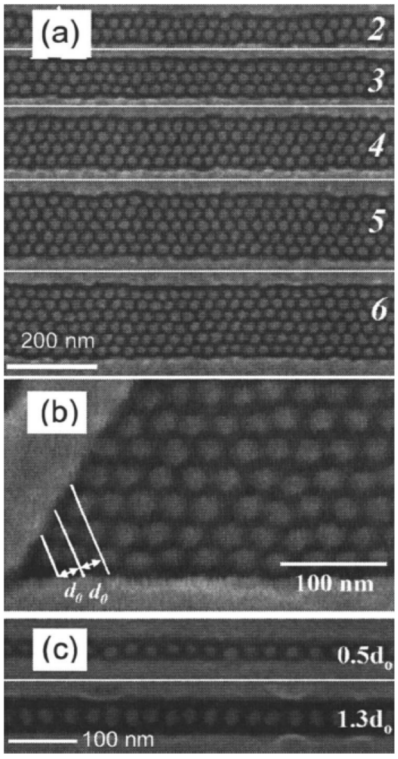

Figure 10: Self-assembled PS-PFS 33/10 patterns. a) In grooves of different widths, a composite image from Ref. 17, b) in a 60° angle from Ref. 22, c) in narrow grooves, showing ellipsoidal distortion of the PFS microdomains from Ref. 34. In each case the PS matrix has been selectively etched. Source [20].

Tip Based Lithography

Tip based methods have demonstrated atomic level precision with their ability to address individual atoms of a surface with the scanning tunneling microscope (STM) tip. Atoms are preferentially displaced from a passivated surface to expose a chemically active under layer (typically silicon). This reactive surface is further used to deposit a hard mask

and subsequently etch into the substrate to create atomically precise shaped structures [23]. This technique is largely confined to research due to very low throughput.

FRAMEWORK FOR NANOSHAPE STUDY

As discussed above, a gap exists in the fabrication of complex nanoshapes at high throughputs required in volume manufacturing for emerging applications, which imprint lithography has the potential to fill. This work is an effort to satisfy this need by the following framework consisting of fabrication, modeling and metrology.

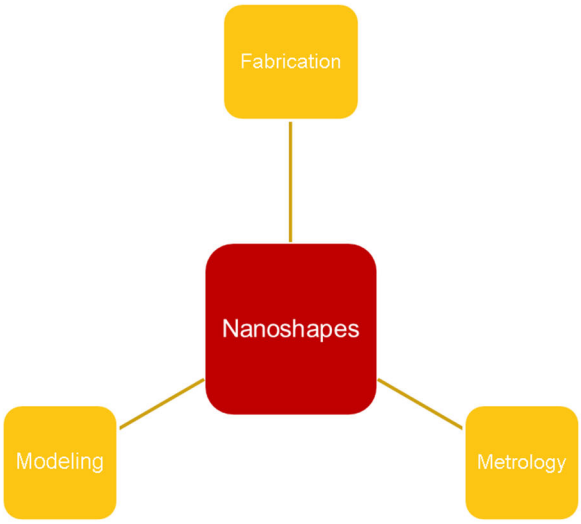

Figure 11: Three pronged framework to study nanoshapes.

The next part (Chapter 2) investigates fabrication of a diamond-like nanoshape using a standard imprint mask and atomic layer deposition (ALD) technique. The pattern created by imprint replication has then been used to fabricate silicon nanowires for ultracapacitor application (a collaborative effort with other graduate students). The focus

of chapter 2 includes experimentally understanding the fundamental behavior and shape retention limits in sub-100nm shaped resist structures such as sharp corner radius increase and break down of continuum material assumptions near sub 5nm domains.

A molecular dynamics (MD) based atomic modeling effort is discussed next (Chapter 3 & 4) to better understand and model the above experimental observations not explained satisfactorily by a continuum mechanics material model. The MD model requires no a priori assumptions about resist material properties and therefore smoothly transitions from the continuum domain to the molecular domain. This sophisticated aspect is fully leveraged in this work by using MD to *Design for Nanoshape Retention (DNR)*. DNR entails predicting resist properties, shape retention and thus help design the imprint template with shape retention features similar to optical proximity correction (OPC) on photomasks [8].

Metrology is the link between experiment and modeling. A few novel metrology methods are employed to accurately measure sub 5nm dimensions and will be discussed in the appropriate sections.

Chapter 2: *Fabrication of Nanoshapes*[4]

The first challenge of nanoshapes was identifying a novel combination of established processes to fabricate an imprint template containing shaped structures. This is because conventional mask fabrication by e-beam lithography is limited to ~10nm resolution, as explained earlier. Once such a nanoshape template is available, the crucial imprint replication step can be performed. The replicated structures will be compared to the corresponding features on the template and the capability of the process to faithfully reproduce the template shape will be evaluated.

ALD BASED FABRICATION OF IMPRINT TEMPLATES

Since the typical method of template fabrication with e-beam lithography [24] is not feasible, a new method to create large area nanoshapes with sub-3 nm sharp corners was adopted to fabricate a four-pointed diamond shape. The sharp pointed nanoshapes are fabricated as follows. A fused silica template containing 100 nm circular pillars of a 200 nm pitch on a square grid is created from a master template containing the opposite tone (circular holes) by a standard imprint replication. Atomic layer deposition (ALD), a conformal and self-limiting deposition technique, is used to increase the lateral dimensions of the pillars one atomic layer at a time [25]. The ALD work was done on a Cambridge Fiji deposition tool. The ALD process works as follows. The substrate, in this case a six inch glass imprint template with etched patterns, is placed on a carrier plate and loaded into the

[4] Portions of this chapter are published in IEEE Transactions on Nanotechnology, vol. 15, Issue 3, pp 448-456, May 2016 in the article titled "Nanoshape Imprint Lithography for Fabrication of Nanowire Ultra-capacitors" with the authors being A. Cherala, M. Chopra, B. Yin, A. Mallavarapu, S. Singhal, O. Abed, R. Bonnecaze and S.V Sreenivasan. A. Cherala performed the template fabrication, imprint replication, AFM and some SEM measurements. M. Chopra performed FEA simulations, some SEM measurements and related data analysis. B.Yin and A. Mallavarapu worked on ultra-capacitor fabrication and measurements. S. Singhal and O. Abed provided process support for imprinting, mask fabrication and metrology. R. Bonnecaze and S.V Sreenivasan supervised the research work.

reaction chamber. The carrier plate and surrounding chamber are kept at 110 °C. The chamber is maintained nominally at 200 mbar pressure. For SiO2 deposition the precursor is TrisdimethylaminoSilane (TDMS). The reaction is completed by flowing oxygen plasma that displaces the methyl groups and leaves a new layer of silicon dioxide and hydroxyl group on the surface. The reaction is continued by repeating the cycle for the desired film thickness. The deposition rate was measured to be 0.75-0.8 Å per cycle.. By gradually increasing the diameters of the pillars until two adjacent pillars touch, diamond shaped holes are formed at the interstitial region of a set of four pillars. This results in a template with features with atomically sharp tips for imprinting.

In order to directly image the template under a scanning electron microscope (SEM), ALD was performed using two different materials. A 20 nm thick layer of titanium nitride (TiN) was first deposited on the glass template because it is conductive and reasonably transparent to UV (a requirement for eventually imprinting with the template). The ALD procedure is followed for TiN deposition with a tetrakisdimethylamido-titanium precursor and an ammonia based plasma to provide the nitrogen species. A capping layer of silicon dioxide (glass) was then deposited on top of the TiN, also using ALD. The deposition of the TiN is essential to dissipate charge for the high resolution imaging of the template. Without the conductive TiN film, imaging the fused silica template would have led to substrate charging during inspection by the SEM, significantly deteriorating image information and making shape measurements impossible. Accurate deposition of the ALD films to build the sharp corners is also enabled by high quality imaging of the template. In addition, results show that the template survives the standard template cleaning process that involves aggressive acid based cleaning required by the protective capping layer of glass. This is important for repeated use of this layered template for scalable fabrication. A

photograph of the prepared template is shown in figure 12. The golden color is due to the TiN film. Patterned areas are visible near the center of the 6" template. The figure also shows SEM images of the pillar structures with gaps visible between them. These images were taken at an intermediate step with further ALD deposition required to make the pillars touch. The high quality imaging is made possible by the conductive TiN layer.

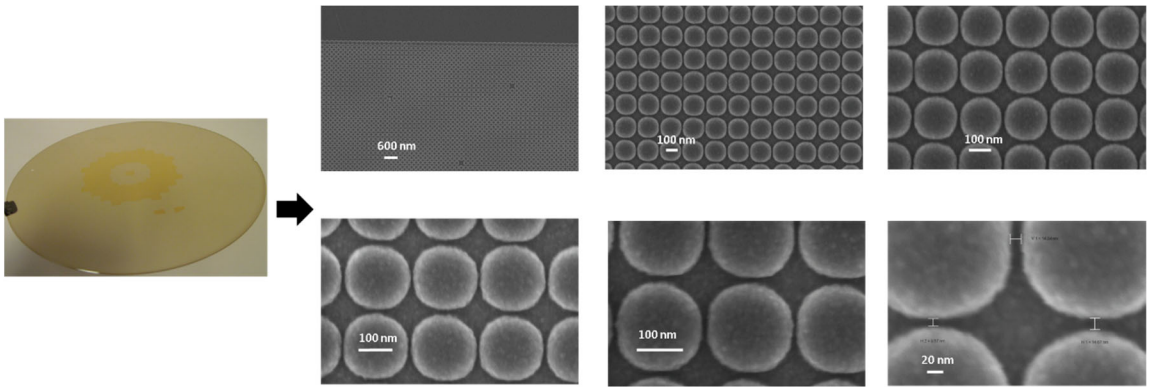

Figure 12: TiN coated template and associated SEM images. The conductive TiN enables accurate SEM imaging by dissipating electron charge from the substrate.

The radii of the sharp corners formed after final ALD are between 2.5-3.5 nm making them an ideal geometry for studying replication of nanoshapes. Also, in addition to the sharp corners, narrow gaps between the pillars are created from location errors and diameter variations of the pillars. These gaps, along with sloped sidewalls (typical of features created with reactive ion etching), create complex 3D "nanoscapes" on the template that tests the limits of imprint replication.

NANOSHAPE METROLOGY AND OBSERVATIONS

Imprints were made on an Imprio® -1100 machine on 6-inch silicon wafers coated with ValMat® coating as adhesion layer and Monomat NS-A-M resist material. The resist is non-conductive, so it must be coated with a conductive material to image at high

resolution with a SEM. Typically, a thin film (a few nanometers) of gold or other conductive material is deposited on top of the resist to enable imaging under the SEM. However in this case, even a few nanometers of conductive film prevents the study of the critical corners which itself is below 3 nm. Further, the fabricated nanopatterns are too fragile to withstand the physical effects of sputtering. During imaging, prolonged exposure to the electron beam deforms the polymer making high magnification images extremely difficult to attain. AFM based measurements were made of the sharp corners in the resist structures to overcome these imaging challenges.

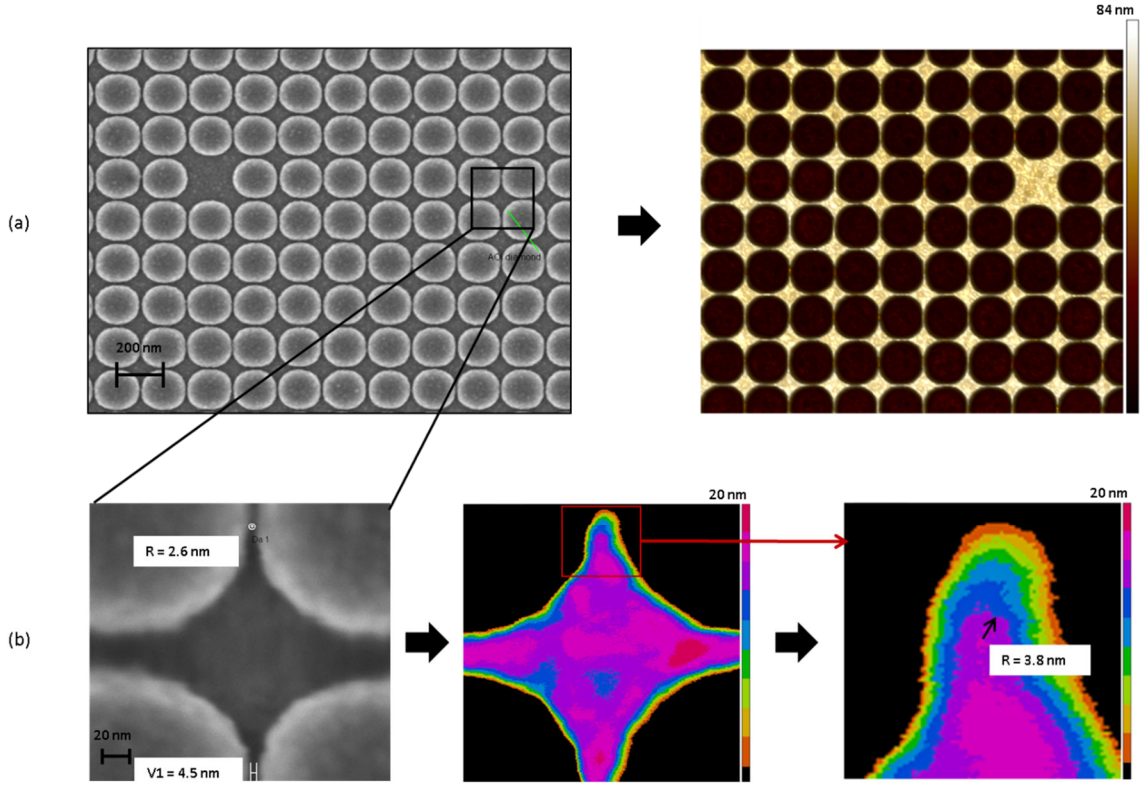

Figure 13: SEM and AFM images a) SEM image of template (left) and corresponding AFM scan of resist showing what appears to be shape retention over larger area (right) b) shows 2.6 nm radius corner on template (left) is replicated in the resist (center) and measured at 3.8 nm radius with AFM(right). The SEM image shows the sharp corner measured at the base of the pillars on the template. The AFM images show the corresponding top of the feature in imprint resist with each color representing a 2 nm horizontal slice; this location represents the ultra-sharp corner of the imprinted resist

Several images of the template and imprinted resist were imaged with SEM and AFM respectively to compare to the model predictions. A finite element model developed to model resist behavior (collaborative effort with another graduate student), accurately predicts the decrease in height and radius of curvature of the side of the diamond as well as the increase in sidewall angle. However, the model predicts a decrease in the corner curvature contrary to experimental results that show an increase in corner curvature as compared with the template shape (Figure 13).

This sharp corner radius increase behavior of imprint resist is being reported here for the first time and determines the ultimate resolution limit of imprint lithography. Reference 11, which comes closest in terms of resolution to the results reported here had a significantly different geometry, namely sub 3nm cylindrical lines (replicated from carbon nanotubes). This difference in geometry makes it difficult to compare with our results, especially the corner radius increase. These results suggest a limit for retaining nanoscale radii of curvature due to the polymer. This is consistent with similar work where it was demonstrated that elastic moduli become inhomogeneous at length scales comprising several tens of monomers [26].

To study the pattern transfer capability of the imprint resist for the diamond, imprints were made on a thermal oxide coated silicon wafer and etched with reactive ion etching to a depth of 30 nm. Imprint etching requires two etch steps. First, an argon-oxygen etch is used to remove the residual layer of imprint resist to expose the underlying substrate. Second, using the imprint resist as a hard mask, the etch into the thermal oxide is done with CF_4, Ar and CHF_3. Etched results show that the sharp corners on the template lose about 2.6 nm due to the etch process as seen going from the template to the imprint resist after residual layer etch, as shown in Figure 14. Thus, the imprinting step with the polymeric

resist sets the ultimate resolution of the patterning process. In addition, this work represents investigation of shape retention over large areas allowing exploration of practical devices such as ultra- capacitors.

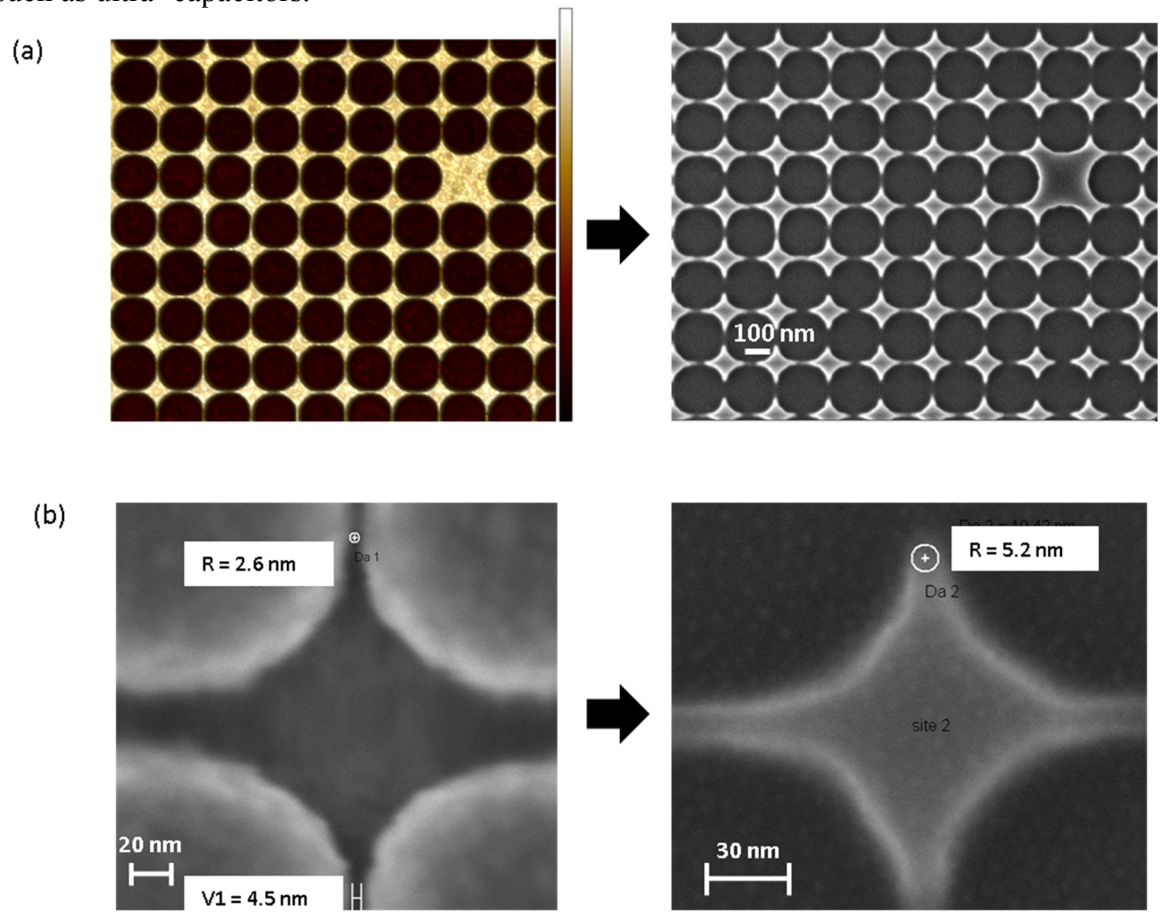

Figure 14: SEM and AFM images a) AFM scan of resist showing what appears to be shape retention over larger area (left) and corresponding features after RIE etch into oxide (right) b) template showing 2.6nm radius corner (left) and etched diamond showing 5.2nm radius corners in oxide (right).

EXEMPLARY NANOSHAPED DEVICE (ULTRACAPACITOR)

Note: The ultra-capacitor fabrication and testing was done primarily by the authors' lab colleagues Dr. Bailey Anderson Yin and Ms. Akhila Mallavarapu. The following section is adapted from ref. [1] with authorship acknowledged appropriately.

Finally, the diamond template is used to form shaped nanowires with sharp corners to produce large arrays of diamond-shaped nanowires, which can be used as enhanced metal-oxide-semiconductor (MOS) capacitors. Here the template in Figure 13 is used to form a diamond pattern with gold followed by a metal assisted chemical etching (MACE) process to create the shaped silicon nanowires [27]. Images of the diamond nanowires are shown in Figure 15. MOS capacitors were fabricated using these diamond-shaped nanowires. The diamond-shaped nanowires have significantly improved specific capacitance compared to circular Si nanowire capacitors.

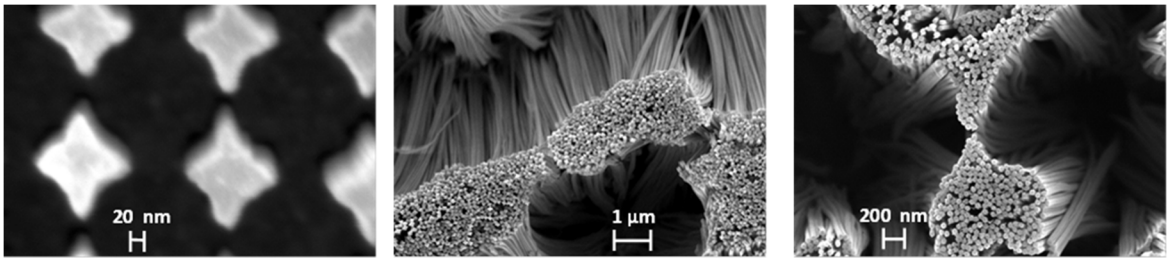

Figure 15: SEM images of diamond-shape nanopatterns: diamond shaped nanowire cross-section (left), high aspect ratio shaped silicon nanowires (center) and circular silicon nanowires (right).

Equation (1) gives the capacitance of a cylindrical capacitor which is a function of its height *h* and the inner *a* & outer *b* radii of the dielectric ring as shown in Figure 16. The equation accounts for the difference in surface area due to the dielectric thickness.

$$C_{cylinder} = \frac{2\pi\varepsilon_0\varepsilon_S h}{\ln(b/a)} \quad (1)$$

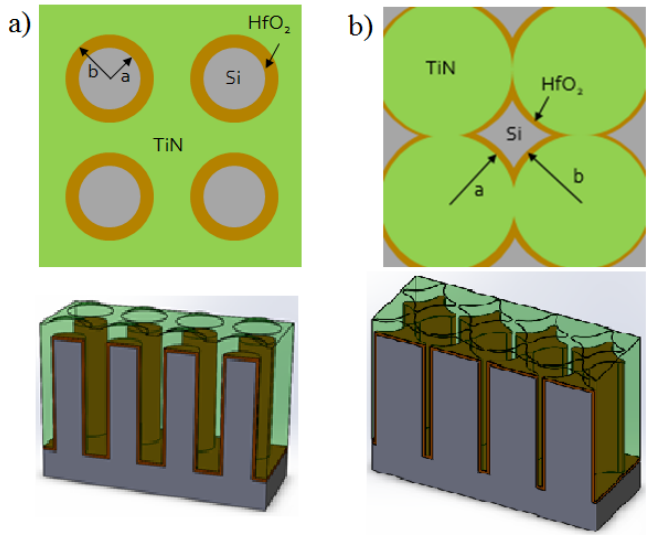

Figure 16: Top and 3D cross-sectional views of (a) Circular cross section capacitor (left) and (b) Diamond cross section capacitor (right); where *a* is the radius of the inner electrode and *b* is the radius of the outer electrode. The thin brown layer is the dielectric (HfO_2), the green bulk material is TiN and the grey wires and substrate are p-Si.

For the capacitors with circular cross section, *a* is 50 nm, and *b* is 61 nm[5]. In the case of the diamond cross section shown in Figure 16b, the calculations were performed using the titanium nitride electrodes which are assumed to be pillars with circular cross sections of 100 nm radius. The projected increase in capacitance for a diamond cross section compared to circular cross section for the same projected area and pillar height was calculated to be ~76%. Forty devices were tested and compared on the basis of capacitance per unit area for a constant nanowire height. These devices were probed to measure C-V characteristics using Capacitance-Voltage (CV) method [28] at a frequency of 5 kHz using the Agilent B1500A semiconductor device parameter analyzer. A representative measurement is shown in Figure 17 along with an SEM image of the capacitor cross section. The capacitance of the diamond nanowires is found to be 18.44 $\mu F/cm^2/\mu m$

[5] The dielectric constant used in the analytical calculations was back calculated using the parallel plate capacitor equation and data from a capacitor with known thicknesses. This was done because the method of deposition can influence the actual dielectric constant value compared to theoretical values.

compared to 9.67 μF/cm^2/μm for circular nanowire capacitors which is 90.62% increase in capacitance per projected area per unit pillar height as shown in Table 1. The dielectric leakage current of the fabricated diamond nanoshaped capacitors was measured to be 10^{-8} A/cm^2 at 3V bias. The experimental capacitance values were slightly less than the expected analytic values which we believe is due to some critical dimension loss compared to the ideal geometries during pattern transfer. Here we have normalized the nanowire capacitor data not only for a unit square area but also for a unit height of the nanowires to allow effective comparison with other similar work reported in literature [29], [30]. The resulting shaped nanowire capacitors not only exceeded the circular nanowire capacitor, but also porous nanocapacitors reported in Reference 29 where they achieved ~10 μF/cm^2/μm. Further, our approach should be scalable to 10X smaller half-pitch nanowires since nanoimprint has demonstrated structures as small as 10nm half-pitch over large areas; this would increase surface area and therefore potential capacitance by an addition ~10X.

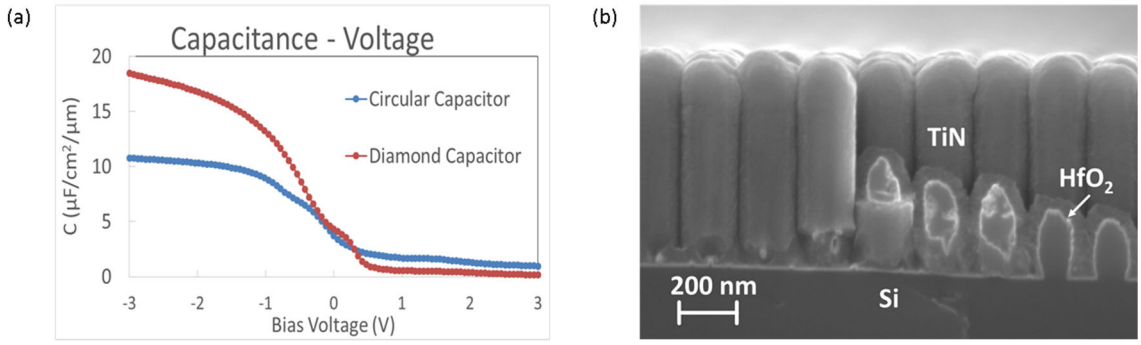

Figure 17: (a) C-V curves comparing the specific capacitance (μF/cm2/μm) of circular and diamond MOS capacitors. (b) SEM cross-section of a capacitor.

Capacitance per Projected Area per unit Pillar Height ($\mu F/cm^2/\mu m$)			
	Circular Nanowire Capacitor	Shaped Nanowire Capacitor	Percent Capacitance Increase of Shaped Nanowire Capacitor
Analytical	12.62	22.24	76.20%
Experimental	9.67	18.44	90.62%

Table 1: Capacitance per projected area per pillar height.

Chapter 3: *Imprint Resist Modeling with Molecular Dynamics*[6]

As part of the ultracapacitor fabrication process, careful measurements were performed to compare the diamond feature on the imprint template and the replicated resist. It was observed that the radius of the sharp corner on the template was larger when measured on the imprinted resist feature (Figure 13). A finite element model used to estimate the resist shrinkage did not capture this behavior. The model, in fact predicted the opposite trend while accurately predicting changes in the larger dimensions of the diamond. The finite element model assumes a uniform elastic modulus and Poisson's ratio which are model inputs, where as it has been reported in the literature that the bulk properties of materials, especially polymers lose homogeneity for dimensions below few monomer lengths [26]. We believe this discrepancy is a key contributor the failure of this model to capture the corner radius increase behavior.

This failure led to the search for a more sophisticated model for the sub 5 nm length scales of interest for nanoshaped structures. Such a model would be an essential design tool, for example to enable scaling of the ultracapacitor density with 10 nm half pitch shaped structures, as mentioned earlier. The following section discusses a survey of modeling schemes available and why all atom MD was chosen. A brief description of MD modeling method is followed by imprint resist modeling and validation. Finally, the sharp corner behavior is simulated.

---

[6] Portions of this chapter are published in Microsystems and Nanotechnology, Vol 4, Article 3, Apr 2018 in the article titled, "Molecular Dynamics Modeling Framework for Overcoming Nanoshape Retention Limits of Imprint Lithography" with authors being A. Cherala, S.V Sreenivasan. A. Cherala performed all the research work reported in this article. S. V Sreenivasan supervised the research.

SURVEY & SELECTION OF MODELING DOMAIN

Figures 18 and 19 show the various modeling frameworks available, bookended by electronic methods at the 10^{-12} m scale to continuum methods at 1.0 m scale.

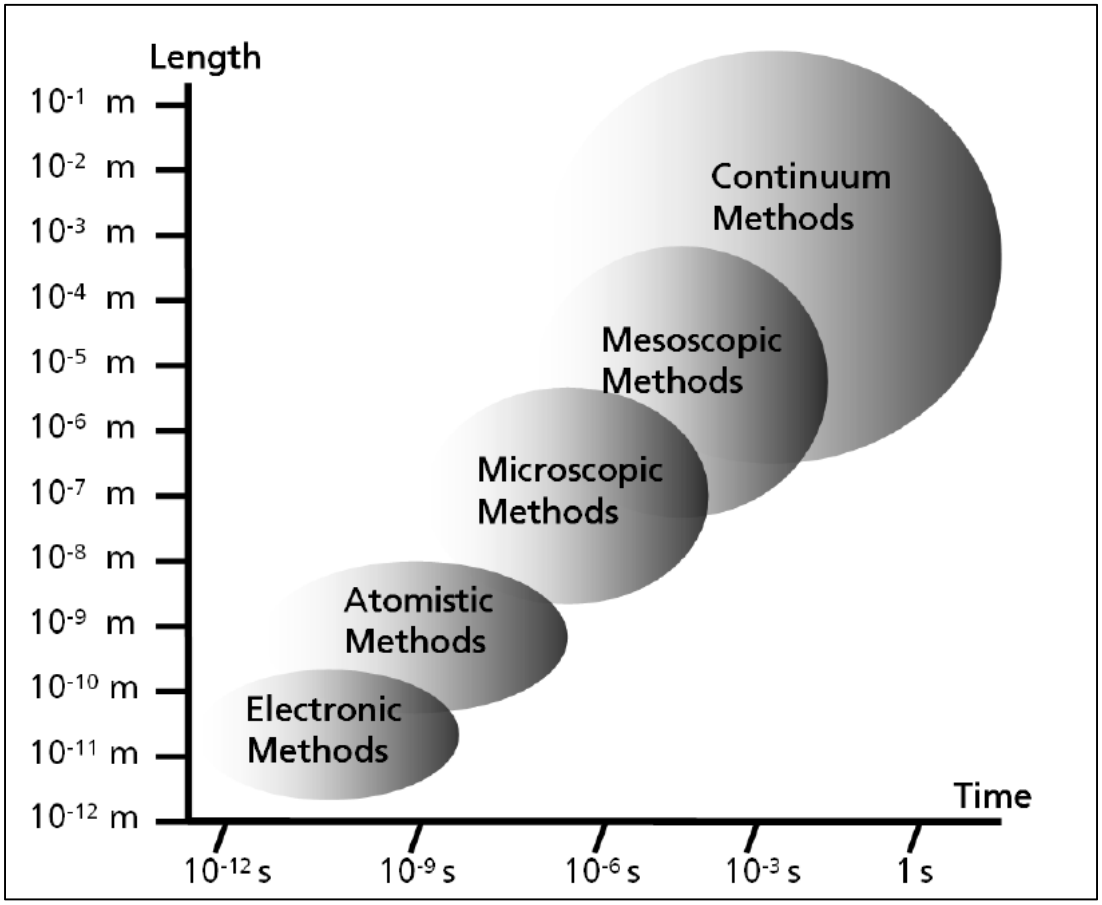

Figure 18: Range of different relevant length and time scales in computational materials science. Source [31].

Scale (m)	Typical Simulation Methods	Typical Applications
Electronic/ Atomistic		
$\sim 10^{-12} - 10^{-9}$	Self-Consistent Hartree-Fock (SC-HF)	crystal ground states
$\sim 10^{-12} - 10^{-9}$	Self-Consistent DFT (SC-DFT)	NMR, IR and UV spectra
$\sim 10^{-12} - 10^{-9}$	Car-Parinello (ab initio) Molecular Dynamics (CPMD)	molecular geometry entropy, enthalpy
$\sim 10^{-12} - 10^{-9}$	Tight-Binding (TB)	electronic properties
$\sim 10^{-12} - 10^{-9}$	Quantum Monte Carlo (QMC)	chemical reactions tribology, dipole moments
Atomistic/ Microscopic		
$\sim 10^{-9} - 10^{-6}$	Molecular Dynamics (MD) and	equations of state
$\sim 10^{-9} - 10^{-6}$	Monte Carlo (MC) using *classical* force fields	Ising model bulk transport properties
$\sim 10^{-9} - 10^{-6}$	Hybrid MD/MC	viscosity
$\sim 10^{-9} - 10^{-6}$	Embedded Atom Method (EAM)	rheology of fluids
$\sim 10^{-9} - 10^{-6}$	Particle in Cell (PIC)	phase equilibrium polymers, DNA models biomaterials charged materials
Microscopic/ Mesoscopic		
$\sim 10^{-8} - 10^{-1}$	MD and MC using *effective* force fields	complex fluids soft matter
$\sim 10^{-9} - 10^{-3}$	Dissipative Particle Dynamics (DPD)	granular matter
$\sim 10^{-9} - 10^{-3}$	Phase Field Models	fracture mechanics
$\sim 10^{-9} - 10^{-3}$	Cellular Automata (CA)	grain growth
$\sim 10^{-9} - 10^{-4}$	Mean Field Theory (MFT)	phase transformations
$\sim 10^{-6} - 10^{2}$	Finite Element Methods (FEM) including microstructure	polycrystal elasticity polycrystal plasticity
$\sim 10^{-6} - 10^{2}$	Smooth Particle Hydrodynamics (SPH)	diffusion
$\sim 10^{-9} - 10^{-4}$	Lattice-Boltzmann Method (LBM)	interface motion
$\sim 10^{-9} - 10^{-4}$	Dislocation Dynamics	dislocations
$\sim 10^{-6} - 10^{0}$	Discrete Element Method (DEM)	grain boundaries
Mesoscopic/ Macroscopic		
$\sim 10^{-3} - 10^{2}$	Hydrodynamics	macroscopic flow
$\sim 10^{-3} - 10^{2}$	Computational Fluid Dynamics (CFD)	macroscopic elasticity
$\sim 10^{-6} - 10^{2}$	Finite Element Methods (FEM)	macroscopic plasticity
$\sim 10^{-6} - 10^{2}$	Smooth Particle Hydrodynamics (SPH)	fracture mechanics
$\sim 10^{-6} - 10^{2}$	Finite Difference Methods (FDM)	aging of materials
$\sim 10^{-6} - 10^{0}$	Cluster & Percolation Models	

Figure 19: Common classification of length scales in materials science. Displayed are also typical scopes of different simulation methods and some typical applications. Source [31].

The quintessential continuum method used especially for solids is the finite element method (highlighted) and has already been shown to fail for our purposes.

The modeling requirements for advanced lithography are listed below:

- Model sub 3 nm length dimensions *without* a priori assumptions of material properties
- Model relaxation and interaction dynamics at useful range temperature and pressures (this is to differentiate from a lot of atomic models that only work at zero Kelvin or in a perfect vacuum)
- Scalable to at least 1 order of magnitude in length & few orders in time
- Model a variety of materials in uniform framework
  - Polymers (resist)
  - Ceramics (fused silica, SiC, SiN, Alumina, Sapphire)
  - Metals/semiconductors (Si, InP, GaAs, Au)
- Results should be easily validated by corresponding experiment data – bulk and nanoscale.

INTRODUCTION TO MOLECULAR DYNAMICS

Due to the aforementioned failure of the continuum mechanics based model, an all-atom classical MD framework was chosen to model the imprint resist, after conducting a survey of models in the nanoscale regime.

The atomic model is expected to accurately capture polymer resist behavior in the below 5 nm and predict a wide range of properties with minimal a priori assumptions regarding material properties, while still being computationally affordable. Bulk material properties will in fact be an output from this MD model. Various degrees of so called

coarse-graining can be done in MD by lumping several atoms or clusters into one effective mass [32]. The coarse grained models reduce the number of masses and therefore reduce computational cost. It was decided not to use coarse graining but instead model each atom in the resist monomer molecules, since the dimensions of interest for nanoshape retention in resist are of the order of the size of a single molecule of monomer.

Modeling atoms and molecules

In all-atom MD, atoms are modeled as point particles with mass and optionally electric charge. The masses assigned are the atomic weights of the respective atom types. Even neutral molecules have partially charged atoms due to electron clouds getting pulled towards the heavier nuclei. Atom connectivity is defined by the topology of the molecule. Bonded connections are modeled as "springs" (linear and non-linear). The spring properties are part of the so called forcefield.

Interatomic Forces

Interatomic forces details are stored in the forcefield, which has been derived from quantum mechanics (ab initio methods). For classical MD, the forcefield is taken as input to the model. The bonded interactions modeled are bond, angle, dihedral and improper types as shown exemplarily in Figure 20.

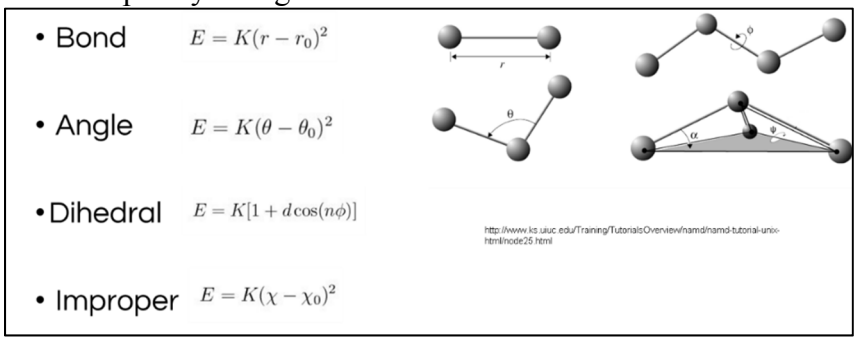

Figure 20: Forcefield bonded interaction models.

Non-bonded interactions are divided into Van der Waals and electrostatic components. The Van der Waals interactions is modeling using a Lennard-Jones potential function and the electrostatic component with a Coulomb potential as shown in Figure 21.

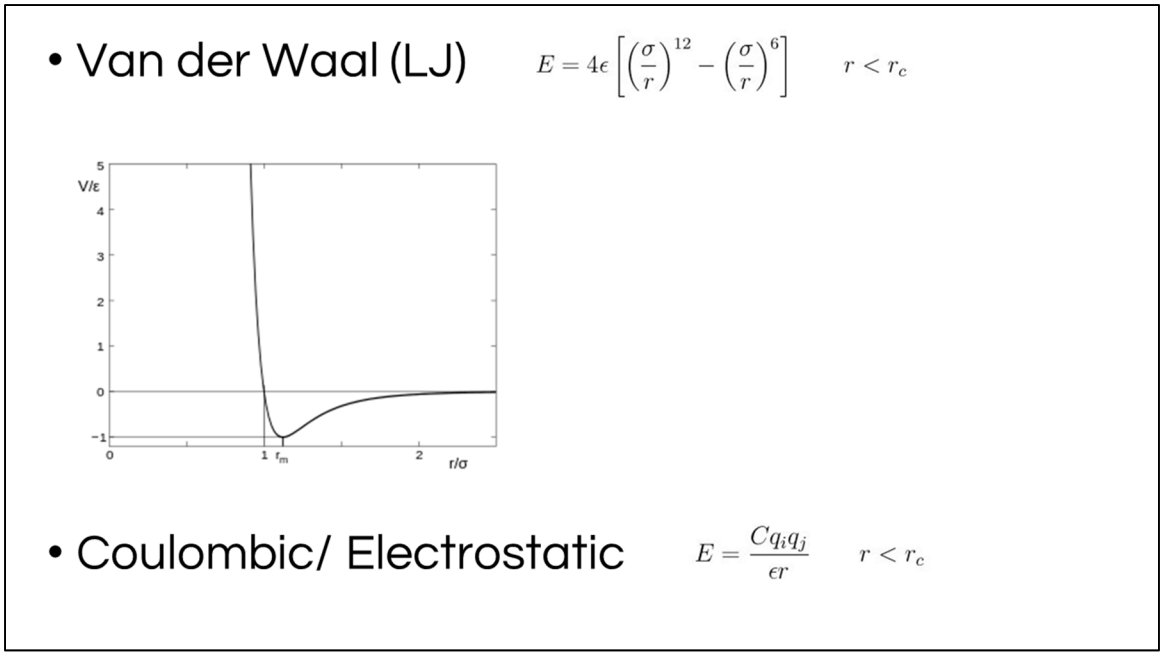

Figure 21: Forcefield non-bonded interaction models.

Energy Minimization

As can be seen, the potential energy of such a system is a function of the atom co-ordinates and forcefield parameters only. MD dynamics simulations are generally started after an energy minimization is performed. This is because starting configurations (and thus atom positions) generated by molecule sketching or lattice placement can create very large forces on atoms mostly due to the non-linear nature of some of the interactions. When the timestepping of the dynamics starts, these atoms are liable to "fly off" and create a missing atoms or stretch bonds to unrealistic limits.

Energy minimization is performed by well-known algorithms like steepest descent, conjugate gradient or Newton Raphson methods. Figure 22 shows a simple example of hexyl acrylate molecule before and after energy minimization.

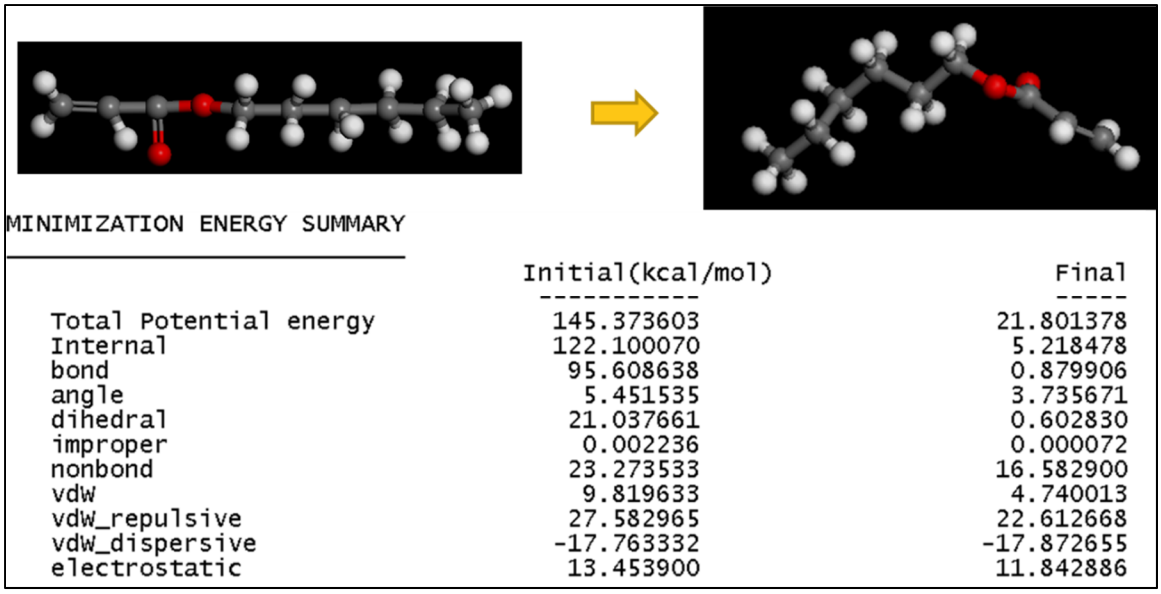

MINIMIZATION ENERGY SUMMARY

	Initial(kcal/mol)	Final
Total Potential energy	145.373603	21.801378
Internal	122.100070	5.218478
bond	95.608638	0.879906
angle	5.451535	3.735671
dihedral	21.037661	0.602830
improper	0.002236	0.000072
nonbond	23.273533	16.582900
vdW	9.819633	4.740013
vdW_repulsive	27.582965	22.612668
vdW_dispersive	-17.763332	-17.872655
electrostatic	13.453900	11.842886

Figure 22: Energy Minimization of hexyl acrylate molecule.

Dynamics

Atom initial velocities are a function of temperature as given by equation 2. A Gaussian distribution of speed (with net momentum = 0, to prevent entire system from drifting) is assigned to the atoms.

$$KE_{avg} = \overline{\left[\frac{1}{2}mv^2\right]} = \frac{3}{2}k_B T \qquad (2)$$

Where,

KE_{avg} = average kinetic energy of the system of particles

m = mass of particle

v = velocity of particle

k_B = Boltzmann's constant

T = temperature

Note that the forcefield (from quantum mechanics) and atom velocity profile (from statistical mechanics/ kinetic theory) are the only inputs to the model. No other material properties are input, rather they are derived from the MD model. This capability of MD is powerful at the nanoscale.

Time stepping is typically performed by a velocity Verlet algorithm. The time stepping equations are shown exemplarily in Equation 3 below.

$$x(t+\Delta t) = x(t) + v(t)\Delta t + \frac{1}{2}a(t)\Delta t^2$$
$$v(t+\Delta t) = v(t) + \frac{a(t) + a(t+\ \Delta t)}{2}\Delta t \quad (3)$$

Where,

x(t) = position of particle at time, t.

v(t) = velocity of particle at time, t.

a(t) = acceleration of particle at time, t.

Δt = timestep of computation.

According to equation 3, the position and velocity of the particle at time t, x(t) and v(t) respectively are known (either from initial conditions or the previous time step). The forces on the particle, which are a function of position, are then calculated according to the forcefield. The acceleration of the particle is then the force divided by its mass, yielding

a(t). Therefore, the position of the particle at time (t + Δt) namely, x(t + Δt) can be calculated. This is in turn used to calculate a(t+ Δt) in the second part of equation 3, to give v(t+ Δt). This procedure is then repeatedly use to perform the time integration. It should be noted here that the while other time stepping algorithms like 4th order Runge-Kutta methods exist, the velocity Verlet algorithm has been shown to track the "ghost" Hamiltonian of the system for extended time periods thus guaranteeing stability while being computationally affordable.

Pressure is defined at the atomic scale by a virial expansion [33] as shown in Equation 4.

$$P = \frac{Nk_BT}{V} + \frac{\sum_i^N x_i . f_i}{dV} \quad (4)$$

Where,

P = pressure

N = number of atoms/particles in the system

V = volume of system

x_i = position of atom *i*

f_i = force on atom *i*

The discerning reader might observe that the position of atoms x_i, appears directly in the dot product in the above equation. So, does the calculated pressure then depend on the selection of origin of co-ordinates? This is not the case, because addition of an arbitrary Δx term would not contribute as the sum of forces (on all atoms in the system) = 0, or in other words $\sum(x + \Delta x).f = \sum (x.f) + \sum (\Delta x.f) = \sum (x.f) + \Delta x. \sum f) = \sum (x.f)$, since $\sum f = 0$. Common MD "fixes" or thermodynamic control actions include barostatting by adjusting

simulation box volume to achieve pressure setpoint and thermostatting by adjusting particle velocities to achieve temperature setpoints.

Operational Details with a simple system (hexyl acrylate molecule)

The main aim of this modeling effort is to simulate behavior of imprint resist. The imprint resist is an organic multi-component material. Each component is first created in Materials Studio (MS) software sold by Accelrys (now Biovia). This software has a very easy to use GUI that lets the user select atom types and sketch a molecule with the required bonds and topology. MS also has its own MD solver packages and custom forcefields. Each component of the resist is created in this way and a minimum energy structure generated. MS also has a volume packing routine that allows for creation of a multi component block of material with a required density and weight percentages.

A detailed step-by-step procedure to create a molecule in MS, export to Large-scale Atomic/ Molecular Massively Parallel Simulator (LAMMPS) [34] and run a simple MD simulation is explained next. LAMMPS is a popular open source MD software developed and supported by Sandia National Labs. Model visualization is done in JMOL and VMD software packages. Documenting the procedure will save time and prevent future researchers from "reinventing the wheel". Note: The author spent an in-ordinate amount of time inventing this "wheel".

The example molecule chosen is hexyl acrylate.

Step 1: Creating the molecule.

Open MS and select *New > 3D Atomistic Document* from the drop down menu. This creates a blank document. The molecule library of MS contains the most commonly used atom types. Select and sketch the atoms in your molecule. Bond topologies can be

defined between the sketched atoms and atom types. Note: Stick figures are default display style in MS. Right click on the sketched stick figure to change display style to ball and stick type to match the figures shown in this document. The distances and angles between atoms is not important in the sketching step since the minimization step later will re-position the atoms to a minimum energy state.

Step 2: Selecting the forcefield

After the molecule is sketched, save the file and open *Modules* > *Discover* > *Setup*. Here the forcefield and other parameters related to forcefield setup can be chosen. A suitable forcefield from a library is chosen to perform the energy minimization (discussed earlier) and the dynamic timestepping.

Step 3: Minimization

Open *Modules* > *Discover* > *Minimizer* to setup a minimization run and execute the minimization. This will create a new folder and the minimized configuration of the molecule is stored here. As part of the minimization, the different potential energy components from bonded and non-bonded interactions are output. These values will need to match with the energy components generated by LAMMPS after importing.

Step 4: Exporting the file

Molecules are exported to a *.car* format by *File* > *Export*. Two files with *.car* and *.mdf* extension will be created upon exporting.

Step 5: To create a multi-molecule volume of material, repeat Step 1-3 for each molecule in your system and save the minimized molecule files.

Step 6: Creating a volume of resist

To create a volume of monomer resist from the different molecules, create another 3D Atomistic Document like in step 1. Create a volume to pack the molecules in with *Build*

> *Crystals* > *Build Crystal*. This opens a dialog box, type in the dimensions of box, for example 50A x 50A x 50A. Next open *Modules* > *Amorphous Cell* > *Calculation.* This opens a pop up window. Select *packing* option in the task list (other options are *construction* for creating a polymer volume and *confined layer*). Here the different component molecules created in step 4 can be selected along with their Mole Ratio/ weight percentage in the mixture. The target density of the multicomponent resist and other forcefield related parameters maybe selected. Click *run* to start the packing algorithm. The packing may take anywhere from 10 minutes to several hours depending on the size of the volume. Once the volume is populated, save the file. The output of the volume packing also gives some statistics about the energies of the different bonded and non-bonded interactions. These will need to match the numbers generated by LAMMPS later. This file can also be exported to a *.car* format.

Figure 23 shows a screenshot of a sketched hexyl acrylate molecule.

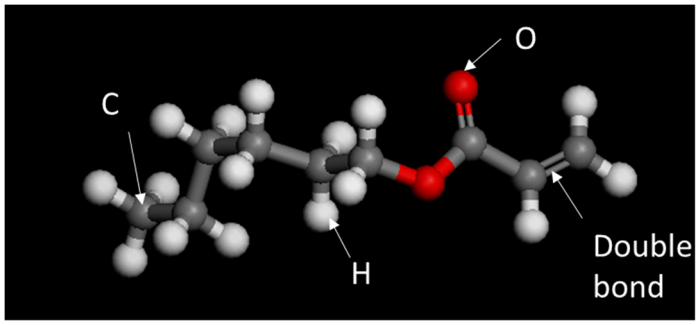

Figure 23: Hexyl acrylate molecule

Step 7: Importing into LAMMPS.

Find the forcefield data file, usually located in *C:\Program Files (x86)\Accelrys\Materials Studio\share\Discover\res*. The file name will be something like cvff.frc. This file along with the *.car* & *.mdf* files are required to convert the MS data to

LAMMPS compatible data. LAMMPS package can be downloaded from http://lammps.sandia.gov/. The package has a data convertor executable called *msi2lmp.exe*. The inputs for this executable are the *.car* & *.mdf* data files and the forcefield file. Please refer to instructions in the LAMMPS package about how to use *msi2lmp.exe*.

Step 8: A data file with extension *.data* is created after successfully running *msi2lmp.exe*. This data file contains all the information about the system including atom positions, charges, bond topology, and force field parameters. This file is directly read into the LAMMPS script. A sample *.data* file of a hexyl acrylate molecule is shown below.

```
LAMMPS data file. msi2lmp v3.9.7 / 24 Oct 2015 / CGCMM for
nhexyl_acrylate_monomer

     27 atoms
     26 bonds
     46 angles
     58 dihedrals
      3 impropers

   7 atom types
  10 bond types
  17 angle types
  19 dihedral types
   3 improper types

    -28.554717730     23.589615901 xlo xhi
    -22.021477635     22.578568185 ylo yhi
    -22.346226820     23.182419172 zlo zhi

Masses

   1  12.011150 # c3
   2  12.011150 # c2
   3  15.999400 # o
   4  12.011150 # c'
   5  15.999400 # o'
   6  12.011150 # c=
   7   1.007970 # h
```

```
Pair Coeffs # lj/cut/coul/long

   1   0.0389999952   3.8754094636 # c3
   2   0.0389999952   3.8754094636 # c2
   3   0.2280000124   2.8597848722 # o
   4   0.1479999981   3.6170487995 # c'
   5   0.2280000124   2.8597848722 # o'
   6   0.1479999981   3.6170487995 # c=
   7   0.0380000011   2.4499714540 # h

Bond Coeffs # harmonic

   1   322.7158     1.5260 # c3-c2
   2   340.6175     1.1050 # c3-h
   3   322.7158     1.5260 # c2-c2
   4   340.6175     1.1050 # c2-h
   5   273.2000     1.4250 # c2-o
   6   400.0000     1.3700 # o-c'
   7   615.3220     1.2300 # c'-o'
   8   322.8000     1.5000 # c'-c=
   9   655.2000     1.3300 # c=-c=
  10   361.6000     1.0900 # c=-h

Angle Coeffs # harmonic

   1    44.4000   110.0000 # c2-c3-h
   2    39.5000   106.4000 # h-c3-h
   3    46.6000   110.5000 # c3-c2-c2
   4    44.4000   110.0000 # c3-c2-h
   5    44.4000   110.0000 # c2-c2-h
   6    39.5000   106.4000 # h-c2-h
   7    46.6000   110.5000 # c2-c2-c2
   8    70.0000   109.5000 # c2-c2-o
   9    57.0000   109.5000 # o-c2-h
  10    60.0000   109.5000 # c2-o-c'
  11   145.0000   123.0000 # o-c'-o'
  12   122.0000   110.0000 # o-c'-c=
  13    50.0000   120.0000 # o'-c'-c=
  14    36.2000   122.3000 # c'-c=-c=
  15    36.2000   120.0000 # c'-c=-h
  16    33.8000   121.2000 # c=-c=-h
  17    37.5000   120.0000 # h-c=-h

Dihedral Coeffs # harmonic

  1     0.1581   1   3 # h-c3-c2-c2
  2     0.1581   1   3 # h-c3-c2-h
```

```
  3     0.1581   1   3 # c3-c2-c2-c2
  4     0.1581   1   3 # c3-c2-c2-h
  5     0.1581   1   3 # c2-c2-c2-h
  6     0.1581   1   3 # h-c2-c2-h
  7     0.1581   1   3 # c2-c2-c2-c2
  8     0.1581   1   3 # c2-c2-c2-o
  9     0.1581   1   3 # o-c2-c2-h
 10     0.1300   1   3 # c2-c2-o-c'
 11     0.1300   1   3 # h-c2-o-c'
 12     2.2500  -1   2 # c2-o-c'-o'
 13     2.2500  -1   2 # c2-o-c'-c=
 14     0.4500  -1   2 # o-c'-c=-c=
 15     0.4500  -1   2 # o-c'-c=-h
 16     0.4500  -1   2 # o'-c'-c=-c=
 17     0.4500  -1   2 # o'-c'-c=-h
 18     4.0750  -1   2 # c'-c=-c=-h
 19     4.0750  -1   2 # h-c=-c=-h

Improper Coeffs # cvff

    1    10.0000  -1   2 # o-c'-o'-c=
    2    11.1000  -1   2 # c'-c=-c=-h
    3    11.1000  -1   2 # c=-c=-h-h

Atoms # full

      1      1   1 -0.300000    -7.248175421     1.027165769    -
1.105747596   0   0   0 # c3
      2      1   2 -0.200000    -6.181919760     0.284273998    -
0.289269715   0   0   0 # c2
      3      1   2 -0.200000    -5.508568708     1.205917106
0.746154767   0   0   0 # c2
      4      1   2 -0.200000    -4.461012522     0.504221402
1.635490733   0   0   0 # c2
      5      1   2 -0.200000    -3.150686702     0.148111311
0.902706792   0   0   0 # c2
      6      1   2 -0.050000    -2.102296566    -0.492994842
1.829716654   0   0   0 # c2
      7      1   3 -0.180000    -0.912774083    -0.857728877
1.079999791   0   0   0 # o
      8      1   4  0.410000     0.099809803     0.080474803
0.903905907   0   0   0 # c'
      9      1   5 -0.380000     0.096942660     1.227518019
1.363489217   0   0   0 # o'
     10      1   6 -0.100000     1.221883200    -0.491290818
0.063031455   0   0   0 # c=
```

```
     11      1   6 -0.200000     2.333426374     0.157441140    -
0.297680242   0   0   0 # c=
     12      1   7  0.100000    -7.725982483     0.359081609    -
1.846226820   0   0   0 # h
     13      1   7  0.100000    -6.817866004     1.877924261    -
1.667293163   0   0   0 # h
     14      1   7  0.100000    -8.054717730     1.428813682    -
0.463738904   0   0   0 # h
     15      1   7  0.100000    -5.424379520    -0.138935891    -
0.976770864   0   0   0 # h
     16      1   7  0.100000    -6.641889291    -0.585975381
0.218670502   0   0   0 # h
     17      1   7  0.100000    -6.290117638     1.637287377
1.401835307   0   0   0 # h
     18      1   7  0.100000    -5.048859488     2.078568185
0.241176698   0   0   0 # h
     19      1   7  0.100000    -4.905343947    -0.399941142
2.096500840   0   0   0 # h
     20      1   7  0.100000    -4.224868591     1.173245222
2.486419559   0   0   0 # h
     21      1   7  0.100000    -2.718565906     1.058035106
0.442254124   0   0   0 # h
     22      1   7  0.100000    -3.356103221    -0.539730237
0.060913172   0   0   0 # h
     23      1   7  0.100000    -2.520852872    -1.409123242
2.288125103   0   0   0 # h
     24      1   7  0.100000    -1.858626426     0.173989364
2.682419172   0   0   0 # h
     25      1   7  0.100000     1.102099158    -1.521477635    -
0.272945661   0   0   0 # h
     26      1   7  0.100000     3.089615901    -0.337515611    -
0.908303574   0   0   0 # h
     27      1   7  0.100000     2.507812609     1.191124500
0.009028123   0   0   0 # h

Bonds

     1   1      1      2
     2   2      1     12
     3   2      1     13
     4   2      1     14
     5   3      2      3
     6   4      2     15
     7   4      2     16
     8   3      3      4
     9   4      3     17
    10   4      3     18
```

11	3	4	5	
12	4	4	19	
13	4	4	20	
14	3	5	6	
15	4	5	21	
16	4	5	22	
17	5	6	7	
18	4	6	23	
19	4	6	24	
20	6	7	8	
21	7	8	9	
22	8	8	10	
23	9	10	11	
24	10	10	25	
25	10	11	26	
26	10	11	27	

Angles

1	1	2	1	12
2	1	2	1	13
3	1	2	1	14
4	2	12	1	13
5	2	12	1	14
6	2	13	1	14
7	3	1	2	3
8	4	1	2	15
9	4	1	2	16
10	5	3	2	15
11	5	3	2	16
12	6	15	2	16
13	7	2	3	4
14	5	2	3	17
15	5	2	3	18
16	5	4	3	17
17	5	4	3	18
18	6	17	3	18
19	7	3	4	5
20	5	3	4	19
21	5	3	4	20
22	5	5	4	19
23	5	5	4	20
24	6	19	4	20
25	7	4	5	6
26	5	4	5	21
27	5	4	5	22
28	5	6	5	21

29	5	6	5	22
30	6	21	5	22
31	8	5	6	7
32	5	5	6	23
33	5	5	6	24
34	9	7	6	23
35	9	7	6	24
36	6	23	6	24
37	10	6	7	8
38	11	7	8	9
39	12	7	8	10
40	13	9	8	10
41	14	8	10	11
42	15	8	10	25
43	16	11	10	25
44	16	10	11	26
45	16	10	11	27
46	17	26	11	27

Dihedrals

1	1	12	1	2	3
2	2	12	1	2	15
3	2	12	1	2	16
4	1	13	1	2	3
5	2	13	1	2	15
6	2	13	1	2	16
7	1	14	1	2	3
8	2	14	1	2	15
9	2	14	1	2	16
10	3	1	2	3	4
11	4	1	2	3	17
12	4	1	2	3	18
13	5	4	3	2	15
14	6	15	2	3	17
15	6	15	2	3	18
16	5	4	3	2	16
17	6	16	2	3	17
18	6	16	2	3	18
19	7	2	3	4	5
20	5	2	3	4	19
21	5	2	3	4	20
22	5	5	4	3	17
23	6	17	3	4	19
24	6	17	3	4	20
25	5	5	4	3	18
26	6	18	3	4	19

```
    27    6      18       3       4      20
    28    7       3       4       5       6
    29    5       3       4       5      21
    30    5       3       4       5      22
    31    5       6       5       4      19
    32    6      19       4       5      21
    33    6      19       4       5      22
    34    5       6       5       4      20
    35    6      20       4       5      21
    36    6      20       4       5      22
    37    8       4       5       6       7
    38    5       4       5       6      23
    39    5       4       5       6      24
    40    9       7       6       5      21
    41    6      21       5       6      23
    42    6      21       5       6      24
    43    9       7       6       5      22
    44    6      22       5       6      23
    45    6      22       5       6      24
    46   10       5       6       7       8
    47   11      23       6       7       8
    48   11      24       6       7       8
    49   12       6       7       8       9
    50   13       6       7       8      10
    51   14       7       8      10      11
    52   15       7       8      10      25
    53   16       9       8      10      11
    54   17       9       8      10      25
    55   18       8      10      11      26
    56   18       8      10      11      27
    57   19      25      10      11      26
    58   19      25      10      11      27

Impropers

     1    1       7       8       9      10
     2    2       8      10      11      25
     3    3      10      11      26      27
```

Please refer to LAMMPS documentation for the data file syntax.

Step 9: Running MD in LAMMPS: A sample LAMMPS script is shown below to setup a MD run with the hexyl acrylate molecule. Please refer to LAMMPS documentation for syntax and command parameter explanations.

```
      log hexyl_acrylate.log

      units real
      atom_style full
      boundary   p

      pair_style lj/cut/coul/cut 9.5

      bond_style      harmonic
      angle_style     harmonic
      dihedral_style  harmonic
      improper_style  cvff

      special_bonds lj/coul 0.0 0.0 1.0

      read_data nhexyl_acrylate_monomer.data

      dump Datom all hexyl_acrylate.xyz

      thermo_style custom step temp etotal press lx ly lz xy xz yz
xlo xhi ylo yhi zlo zhi vol pxx pyy pzz pxy pxz pyz
      thermo  1
      run 0

      min_style  cg    # cg is default
      minimize   1e-5  1e-6  2000  2000  #etol ftol maxiter maxeval


      velocity        all create 298.0 4337 dist gaussian
      neighbor        2.0 bin
      neigh_modify delay 5

      variable pr_npt equal press

      fix  Fnpt  all  npt  temp  298.0  298.0  100.0  iso  ${pr_npt}  1.0
1000.0

      timestep 3.0

run 100
```

Prior to running MD in LAMMPS however, the system energies should be checked against MS values to ensure correct import. This can, for example, be done by selecting the various

bonded and non-bonded energies for output in the thermo_style command as shown below (`etotal, evdwl, ecoul, epair, ebond, eangle, edihed, eimp`) and comparing term by term with MS output for the system in this exact same configuration.

```
thermo_style custom step temp etotal evdwl, ecoul, epair, ebond,
eangle, edihed, eimp, press lx ly lz
      thermo  1
      run 0
```

Please note that the terms differ between MS and LAMMPS. Dihedral is called torsion and improper is called out-of-plane in MS respectively. The *run 0* command enables the system energies to be output as imported, before the atoms are moved by timestepping.

ATOMIC MODELING OF IMPRINT RESIST

The imprint resist formulation was taken from the patent literature [35]. The resist consists of three acrylate molecules namely, hexyl acrylate (55% w/w), isobornyl acrylate (25% w/w) and ethylene glycol diacrylate (20% w/w) as the cross linker, as shown in Figure 24a. The atoms and molecule models were created in Accelrys Materials Studio software. A volume of monomer resist is then generated as described above. The Consistent Valence Force Field (CVFF), originally developed to study organic molecules is used to model the intermolecular interactions [36]. The functional form of the forcefield is shown in Figure 24b. Four bonded interactions namely bond, angle, dihedral and improper interactions are incorporated. Partial charges are assigned to dissimilar bonded atoms. Non-bonded interactions include a Lennard-Jones potential for the Van der Waal interaction and a coulomb interaction for the partial charges. The cut-off distance for non-bonded interactions is set to 9.5Å. The resist system is then imported into LAMMPS MD software.

a)

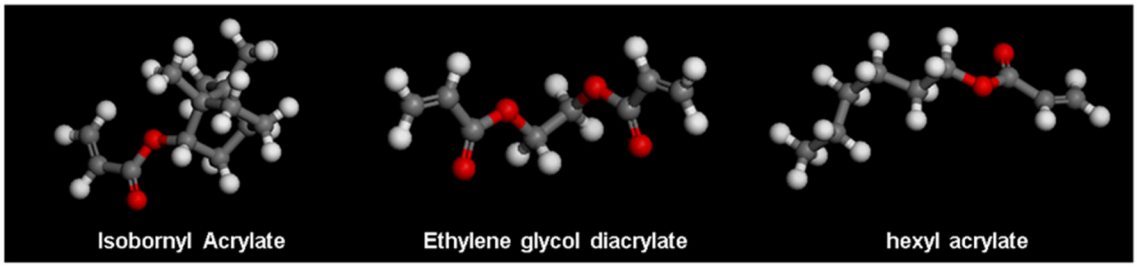

b)

$$E_{pot} = \sum_{bond} k_b(b - b_0)^2 + \sum_{angle} k_\theta(\theta - \theta_0)^2 + \sum_{dihedral} k_d(1 + d.cos(n\emptyset)) +$$

$$\sum_{improper} k_i(1 + d.cos(n\emptyset)) + \sum_{electrostatic} \frac{q_i q_j}{4\pi\varepsilon_0 r_{ij}} + \sum_{Van\ der\ Waals} 4\varepsilon_{ij}\left[\left(\frac{\sigma}{r_{ij}}\right)^{12} - \left(\frac{\sigma}{r_{ij}}\right)^{6}\right]$$

Figure 24: a) Imprint resist components. b) CVFF forcefield functional form.

Chapter 4: *Nanoshapes Modeling with Molecular Dynamics*[7]

RESIST MODEL VALIDATION

MD polymer models may be validated by estimating the bulk resist modulus, strength and glass transition temperature. The liquid monomer model imported from MS is first checked for accuracy by comparing total system energy and the various potential energy components namely bond, angle, dihedral, improper and Van der Waal energies respectively to ensure the atom locations and force interactions were imported correctly into LAMMPS.

The bulk system consists of a 150x150x130Å volume with around 286,000 atoms. The system is first equilibrated in an isothermal-isobaric (NPT) ensemble at 298K and 1 atm. pressure with a Nose-Hoover style thermostat. The time integration is done by a velocity Verlet algorithm at 1 fs intervals. Acrylate polymerization is then performed based on a cutoff distance between two double bond carbons. More specifically, the bond creation step looks for double bonded carbon atoms present within a certain radius. The closest pair is then converted to a single bond and the appropriate molecule topology and bond parameters are updated. This procedure is repeated till there are no more bonds possible. It was observed that the extent of polymerization was around 85-90% which is consistent with numbers reported in literature [37].

The elastic constants of the polymer are estimated by straining the block of material in the three axial and shear directions. The change in stress tensor for each uniform strain component is used to calculate the elements of the 6x6 elastic matrix. The stress-strain

[7] Portions of this chapter are published in Microsystems and Nanotechnology, Vol 4, Article 3, Apr 2018 in the article titled, "Molecular Dynamics Modeling Framework for Overcoming Nanoshape Retention Limits of Imprint Lithography" with authors being A. Cherala, S.V Sreenivasan. A. Cherala performed all the research work reported in this article. S. V Sreenivasan supervised the research.

relationship and form of the elastic matrix for isotropic materials is shown in Equation 5. The values obtained for the polymer

$$\begin{bmatrix}\sigma_{11}\\ \sigma_{22}\\ \sigma_{33}\\ \sigma_{23}\\ \sigma_{13}\\ \sigma_{12}\end{bmatrix} = \frac{E}{(1+\upsilon)(1-2\upsilon)}\begin{bmatrix}1-\upsilon & \upsilon & \upsilon & 0 & 0 & 0\\ \upsilon & 1-\upsilon & \upsilon & 0 & 0 & 0\\ \upsilon & \upsilon & 1-\upsilon & 0 & 0 & 0\\ 0 & 0 & 0 & \frac{1-2\upsilon}{2} & 0 & 0\\ 0 & 0 & 0 & 0 & \frac{1-2\upsilon}{2} & 0\\ 0 & 0 & 0 & 0 & 0 & \frac{1-2\upsilon}{2}\end{bmatrix}\begin{bmatrix}\varepsilon_{11}\\ \varepsilon_{22}\\ \varepsilon_{33}\\ \varepsilon_{23}\\ \varepsilon_{13}\\ \varepsilon_{12}\end{bmatrix} \tag{5}$$

resist are shown in Equation 6. The Young's modulus and Poisson's ratio estimated from the elastic constant is 1.1GPa and 0.42 respectively. These numbers are consistent with numbers reported in the literature for similar materials like PMMA.

$$\frac{E}{(1+\upsilon)(1-2\upsilon)}\begin{bmatrix}1-\upsilon & \upsilon & \upsilon & 0 & 0 & 0\\ \upsilon & 1-\upsilon & \upsilon & 0 & 0 & 0\\ \upsilon & \upsilon & 1-\upsilon & 0 & 0 & 0\\ 0 & 0 & 0 & \frac{1-2\upsilon}{2} & 0 & 0\\ 0 & 0 & 0 & 0 & \frac{1-2\upsilon}{2} & 0\\ 0 & 0 & 0 & 0 & 0 & \frac{1-2\upsilon}{2}\end{bmatrix} = \begin{bmatrix}2.77 & 1.98 & 1.98 & 0.01 & -0.01 & 0.004\\ 1.98 & 2.74 & 1.97 & -0.008 & 0.007 & -0.01\\ 1.98 & 1.97 & 2.74 & 0.009 & 0.012 & -0.006\\ 0.01 & -0.008 & 0.009 & 0.02 & 0.006 & 0.36\\ -0.01 & 0.007 & 0.012 & 0 & 0.35 & -0.01\\ 0.004 & -0.01 & -0.006 & 0.36 & -0.01 & -0.001\end{bmatrix} \tag{6}$$

Polymers are unique in exhibiting a significant change in mechanical properties at the glass transition temperature, T_g. This temperature is estimated by calculating the average volume over a range of temperatures. Figure 25 shows the change in specific volume with temperature. T_g is estimated as the intersection point of the two linear sections of the curve. The value for this polymer system is estimated around 115°C. This compares well for example, with T_g for PMMA reported around 105°C in the literature.

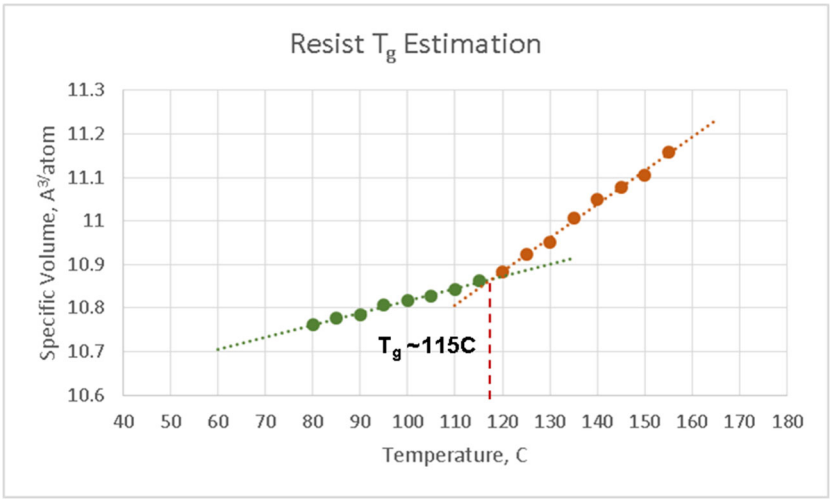

Figure 25: Resist glass transition temperature estimation.

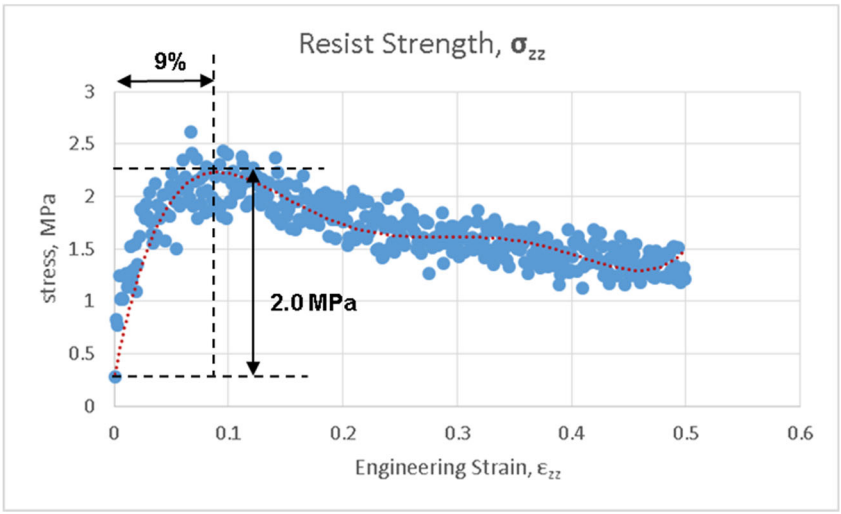

Figure 26: Resist strength estimation by simulated tensile test.

Resist strength is estimated by simulating a tensile test with uniaxial strain and observing peak stress. Figure 26 shows stress from 0 to 50% strain. The yield stress is estimated at around 2.0MPa for 9% elongation based of a polynomial trend line fit. The model validation simulations are computationally very demanding and therefore most of the runs were done on the Texas Advanced Computing Center supercomputers.

SHARP CORNER MODELING

After having rigorously validated the atomic resist model, it can be used to predict shape retention. The 200 nm diamond like nanoshape structure is partially modeled (due to size limitations) in MD as an ideally sharp corner and allowed to time-step for 50ps. The ideal geometric shapes of the imprint template are created in resist by defining primitive shapes like cylinders or rectangular boxes and retaining only the molecules inside or outside of the chosen regions in the system as required. LAMMPS has the capability to create a Van der Waals interaction between the walls of the chosen region and the atoms, so that the walls gently repel the atoms as they get close to the region boundaries. This feature and a careful selection of timestep prevents atoms from moving out of this simulated template nanoshape. After the system is polymerized in this state, the region is removed from the system and the cross-linked resist is allowed to move without restriction. As can be seen in Figure 27, the model is able to qualitatively predict radius increase observed in experiment.

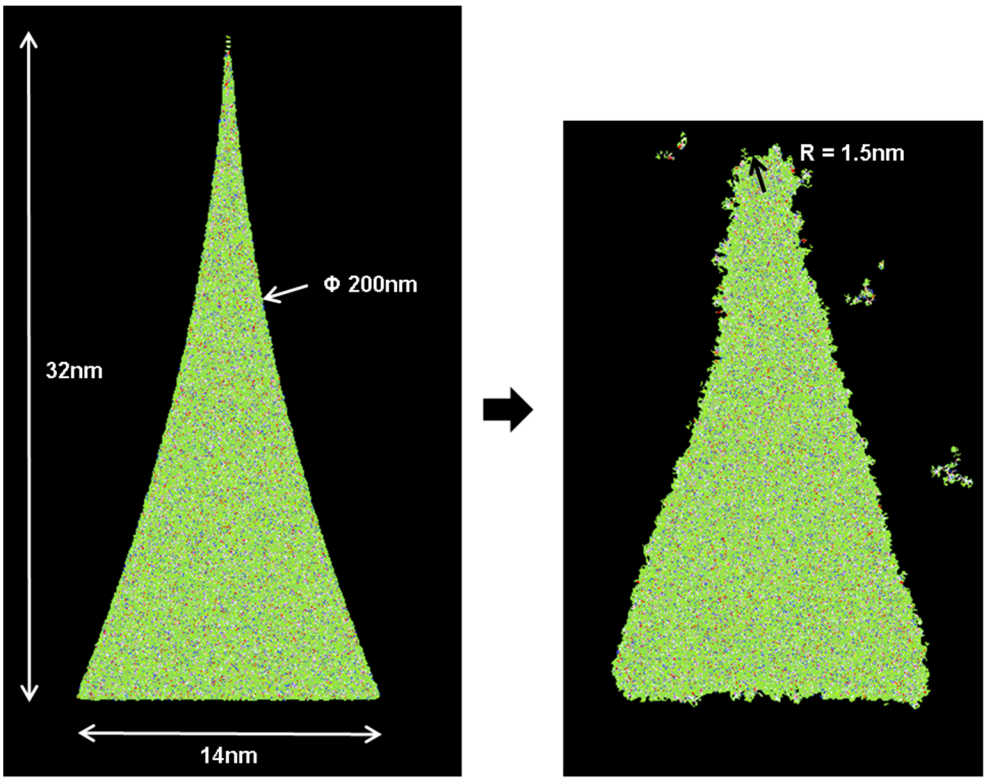

Figure 27: Atomically sharp corner of 200nm diamond like nanoshape (left) and after 50ps simulation (right).

Having thus developed a model that is further validated with experimental data, we can investigate shape retention capability of the resist at the dimensions of interest (below 25nm). To that end, a 25nm and 7.5nm diamond are modeled.

SUB 25NM DIAMOND NANOSHAPE

Figure 28 shows the shape retention after 50ps. As can be seen, the 25nm diamond retains shape except for the sharp corner radius increasing and becoming rounded. The 7.5nm diamond on the other hand, fails to retain the original desired shape. Fig 28c also shows the material dependence on shape retention. The same 7.5nm diamond geometry is

modeled in crystalline silicon with a diamond lattice using the classical Stillinger-Webber multibody potential [38] and fcc crystalline gold using the EAM potential [39]. The two materials retain shape significantly better than polymer resist. The radius of the corners is measured at 0.4nm for silicon and 0.7nm for gold respectively. This shows that the limiting step in the nanoshape fabrication process is shape retention in polymer resist. If the shape is successfully retained in the resist, there should be no problem retaining shape in the underlying hard mask and substrate layers.

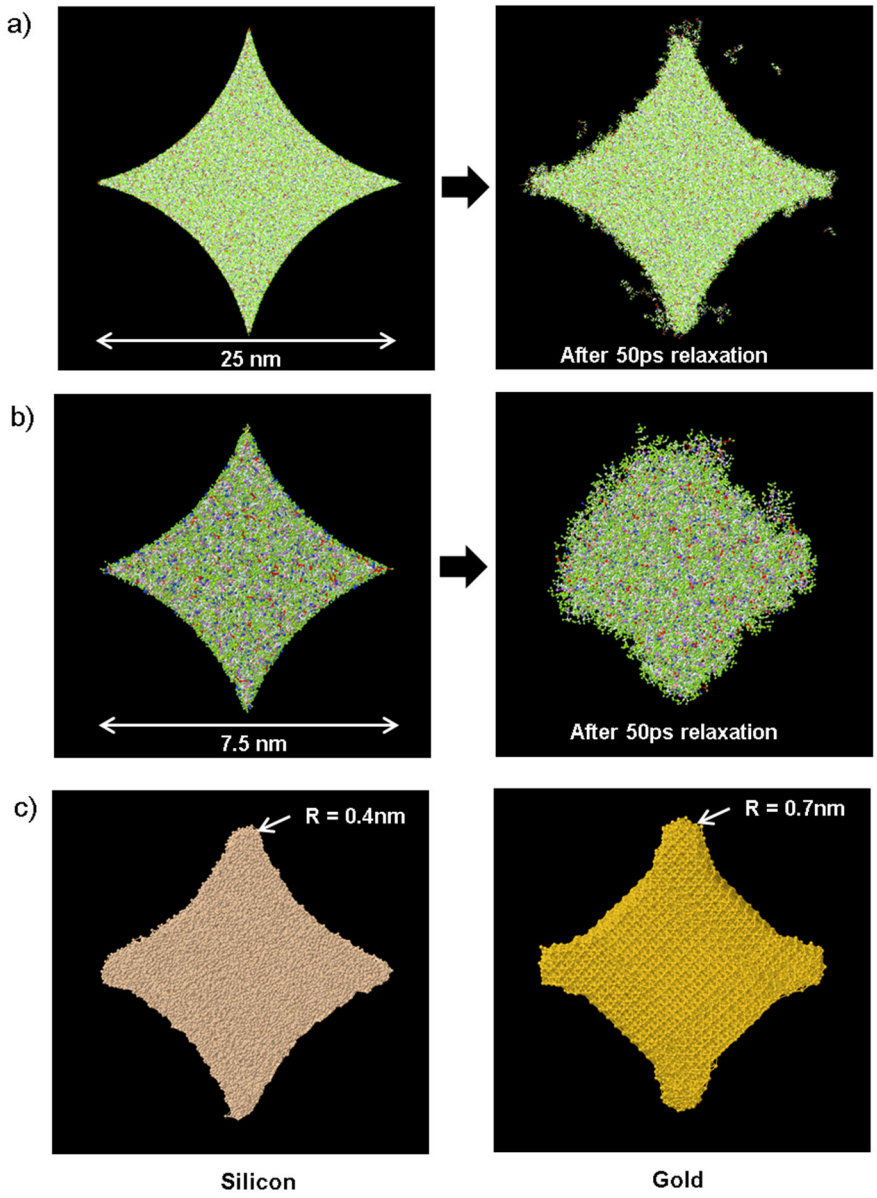

Figure 28: a) Shape retention in 25nm diamond-like nanoshape resist structure b) Failure of shape retention in 7.5nm diamond-like nanoshape resist structure c) same geometry in silicon and gold show significantly better shape retention.

Thus the MD model developed here can be used for optimizing resist material composition, template design, identifying critical dimensions for shape retention and modeling different

materials within a uniform framework. More specifically, for the ultracapacitor application, the model suggests that the 25nm diamond structures are viable whereas the 7.5nm structures are not. This kind of information and analysis, from a first principles based, validated model is a valuable design tool for template and process design. The modeling data minimizes trial and error and costly design of experiments which would otherwise be required to characterize the nanoshape viability. Some ideas to overcome the size limitation for nanoshape imprinting are discussed in the next section.

MD ENSEMBLES AND AVERAGING

In the course of investigation of the nanoshaped structures, the statistical nature of observables becomes evident. For example, the corner radii of the nanoshaped diamond structures in the previous section are not uniform. The variation in radii comes from local non-uniformities in molecular spatial arrangement, bonding efficiencies and local position and velocity (temperature) distributions. Therefore, in order to estimate the corner behavior characteristic of the "average" structure, several different structures, each with unique molecular arrangements can be prepared and simulated. The average radius of the corner can then be calculated from different arrangements. In order to study this approach, five unique 20nm diamond structures were prepared and simulated to 50ps. These 20nm diamond shapes approximately represent a 15nm half-pitch DRAM deep trench capacitor design (see Chapter 6, Fig. 47). Figure 29 shows an exemplar initial diamond structure in inset (a) and the five simulated structures (insets c-f). The average radius is estimated to be ~1.2nm with a standard deviation of ~0.2nm.

The raw data for the twenty measured radii is given in table 2

Ensemble	Corner Radius, nm
1	1.2, 0.8, 1.1, 1.6
2	1.2, 1.4, 1.1, 1.4
3	1.5, 1.1, 1.4, 1.4
4	1.2, 1.2, 1.2, 1.1
5	1.2, 1.0, 1.4, 1.4

Table 2: Corner radii of the five 20nm diamond nanostructures

The average length of a monomer molecule is ~1nm. Assuming this is a characteristic length scale or resolution metric of the problem, it can then be recognized that the 3 sigma variation of the radii predicted by MD simulation is of this order as well (~0.6nm). Also, going back to the original motivation of trying to model polymer relaxation as measured in experiments (Figure 13), the intent was to capture the measured radius increase from the ideal (fused silica template) radius of 2.6nm to the polymer resist radius of 3.8nm. In conclusion, the polymer MD model developed in this work, with an ensemble standard deviation of 0.2nm, should have the resolution to model the dimensional changes observed in the experiments reported in this research.

Statistical analysis can be done on this data set in order to evaluate whether the differences in the mean radii at the four corners are statistically significant (the null hypothesis). To that end, a paired t-test evaluation is done comparing radii at corner 1 to corner 2, 3 and 4 in a pairwise manner. Table 3 shows the raw data, mean, standard deviation and p-value results from the analysis. Since the three calculated p-values are all above the significance level of 0.05, it can be concluded that the difference in the mean radii of the four corners are not statistically significant.

	Corner 1, nm	Corner 2, nm	Corner 3, nm	Corner 4, nm
Ensemble 1	1.2	0.8	1.1	1.6
Ensemble 2	1.2	1.4	1.1	1.4
Ensemble 3	1.5	1.1	1.4	1.4
Ensemble 4	1.2	1.2	1.2	1.1
Ensemble 5	1.2	1	1.4	1.4
Mean	1.3	1.1	1.2	1.4
St. Dev	0.1	0.2	0.2	0.2
P-value two tail (significance level = 0.05)		**0.24**	**0.75**	**0.28**

Table 3: Paired t-test for comparison of mean radius of four corners in 20nm diamond structure

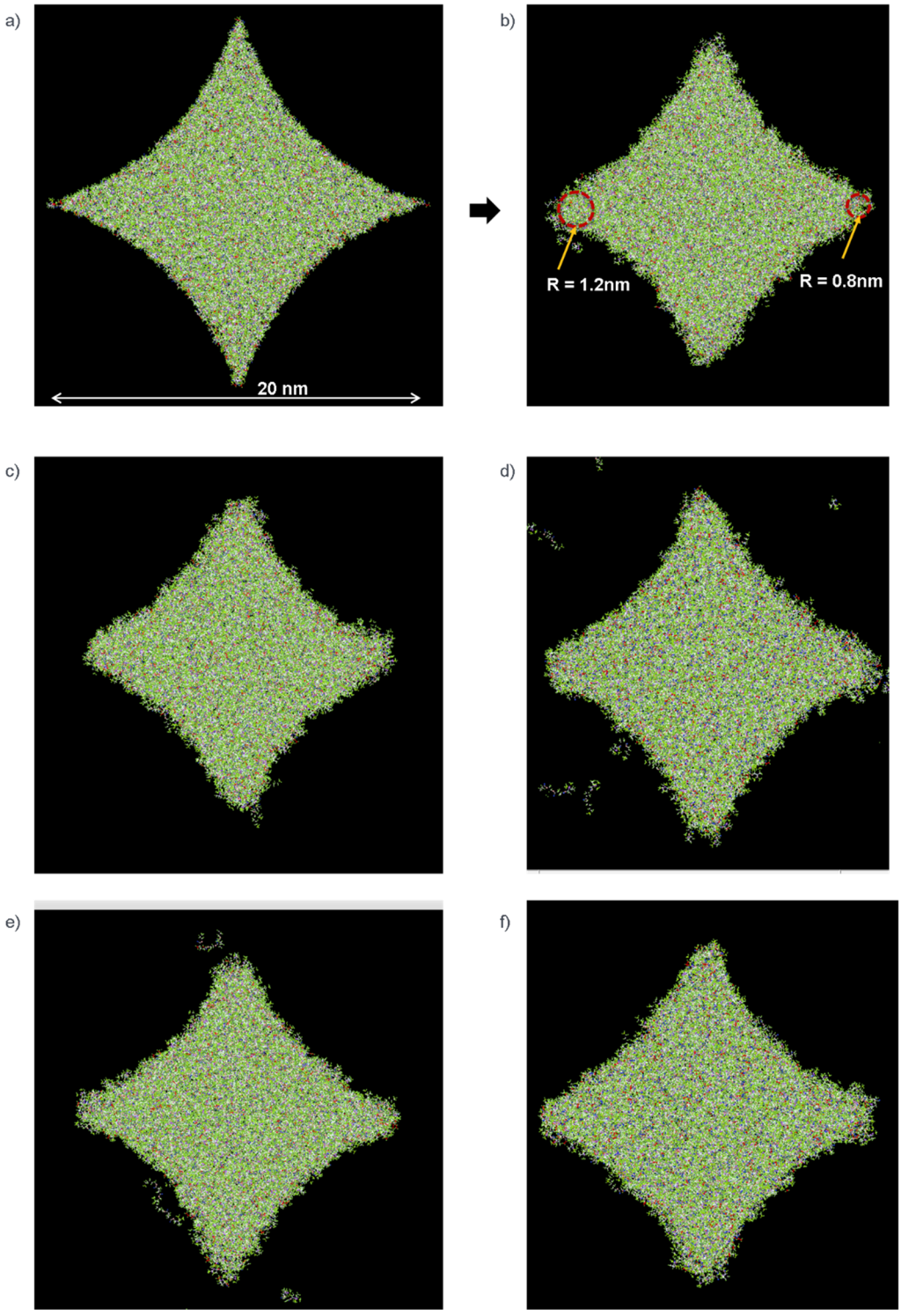

Figure 29: MD Ensembles a) Exemplar 20nm diamond initial configuration. b)-f) five ensembles after 50ps simulation.

DESIGN FOR NANOSHAPE RETENTION (DNR)

Three ideas to improve shape retention are discussed in this section, namely tone inversion, addition of compensating sub-resolution features to the template and exploiting the properties of subsequent RIE etching.

Tone Inversion

Imprint lithography has been practiced in reverse tone, notably in bit patterned media applications and is well established [40]. For nanoshape imprinting, this aspect is very useful and once the critical dimension (for shape retention) for a given geometry is identified following the procedure discussed in the previous section, sub CD features should be pursued in the reverse tone. This is exemplified in Figure 30a, b where a cross nanoshape of size 10x2.5 nm is shown in both tones. Cross shaped nanostructures have potential applications in new memory devices like spin transfer torque RAM [4, 41]. As can be seen, shape retention in the cross feature is very poor. The cross shape retention is better in the reverse tone (cross shaped hole).

Addition of Sub Resolution Features

As can also be seen, while the reverse tone cross retains shape better, it loses original shape due to geometry effects and resist relaxation. Addition of sub resolution DNR features can compensate for this and maintain target cross shape significantly better as shown in Figure

30c. As with other models, the system was run for 50ps. The system energy was tracked and observed to reach steady state after around 5ps. This indicates that the system has reached equilibrium after 50ps. These DNR features are similar to optical proximity correction (OPC) patterns that are well known in optical lithography where they are used to compensate for diffraction and other optical effects at the nanoscale. Here we have demonstrated the design and use of OPC-like features for nanoshape imprint lithography to enhance shape retention by compensating for resist shrinkage, relaxation and other geometry induced effects. Templates can be fabricated with these enhancing features, for example, with STM tip based methods [42].

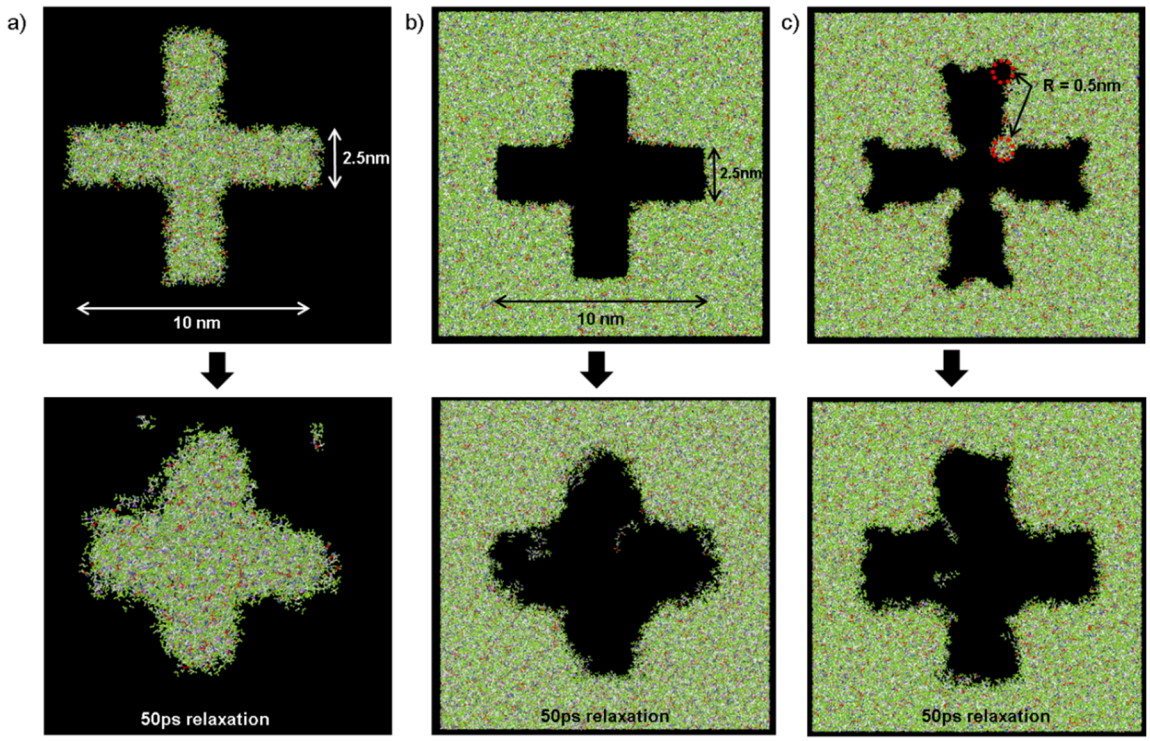

Figure 30: a) 10x2.5nm cross nanoshape resist feature b) Failure of shape retention in 7.5nm diamond-like nanoshape resist structure c) same geometry in silicon and gold show significantly better shape retention.

Etch Compensation

Another aspect of the pattern transfer process that can be exploited is the fact that the reactive ion etch (RIE) process that transfers the shape into the underlying substrate tends to have a small isotropic etch rate. This can be used for example, by designing the template to have a thin connection between adjacent diamond features as shown in Figure 31b. This gap creates a narrow bridge in the imprinted resist. The subsequent etching process breaks down the 3nm bridge leaving a sharper corner when compared to starting with an isolated diamond feature. This phenomenon was exploited with the diamond shape. Figure 31a & b show an isolated diamond with 2.6 nm corner and diamond with a thin connecting bridge (left images) and the corresponding structures after etching into the underlying oxide layer (right images). As can be seen, the bridged diamond shows the sharper corner after RIE, due to the effect explained above.

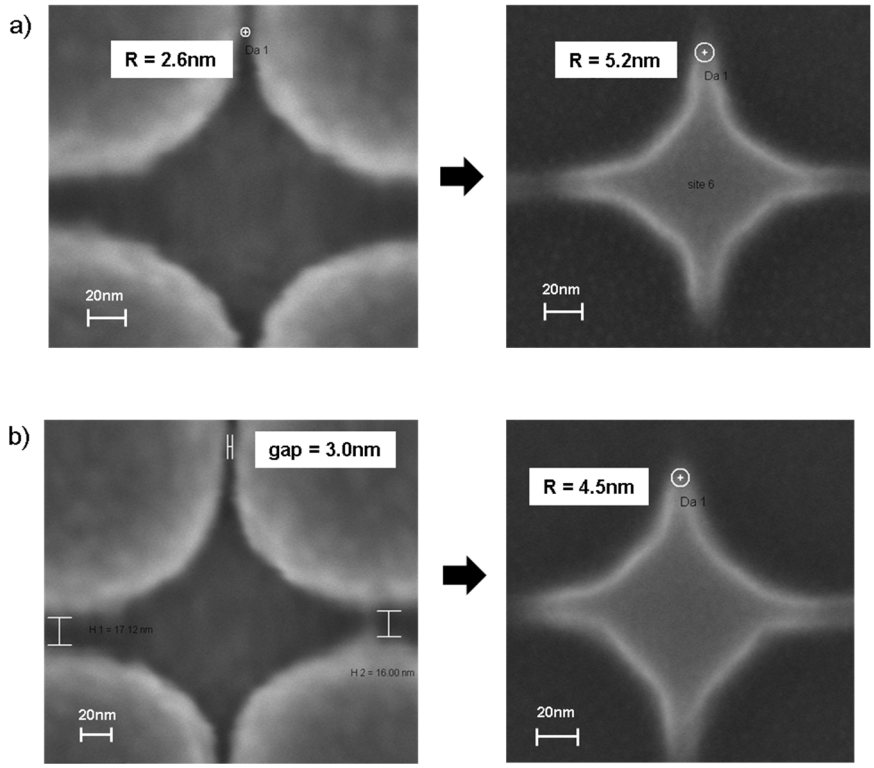

Figure 31: a) SEM image of diamond-like shape template feature (left) with 2.6nm radius corner and corresponding feature after RIE etch (right) into silicon oxide with 5.2nm radius corner. b) SEM image of diamond-like shape template feature (left) with 3.0 nm bridge gap and corresponding feature after RIE etch (right) into silicon oxide with 4.5nm radius corner.

Chapter 5: *Process Integration and Resist Design*

In this chapter, some practical aspects of nanoimprint replication like dry etching, residual layer thickness and template fabrication technology will be addressed in the context of taking advantage of these phenomena for nanoshape fabrication.

POLYMERIZATION IN NANOSHAPED STRUCTURES

Based on the above shape retention results, a key parameter that is expected to influence material modulus and strength in the resist is the polymerization quality and uniformity across the nanoshape. As shown in table 4, the percentage polymerization of bulk (baseline) resist is 87% and two nanoshapes - 7.5 nm diamond and 10 nm cross shapes are at polymerization percentage of 75% and 60% respectively. The shape and size dependence is evident in this data.

Model	Model-Figure	Percentage Polymerization
Bulk (15x15x13nm –periodic b.c)	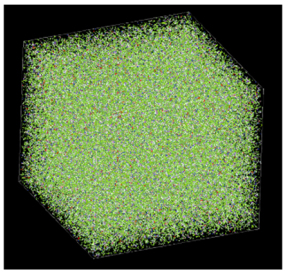	87%

Table 4: continued next page

Model	Model-Figure	Percentage Polymerization
7.5nm Diamond	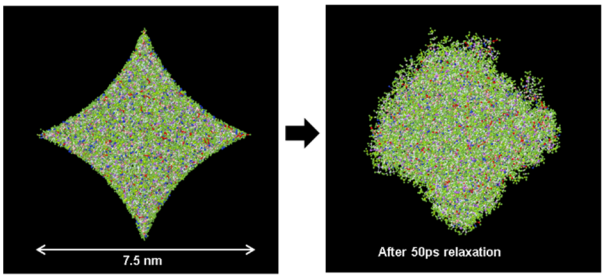	75%
10nm Cross	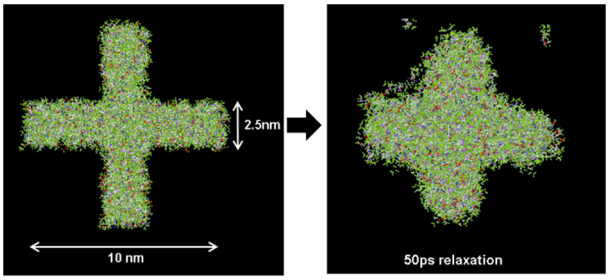	60%

Table 4: Percentage polymerization as a function of nanoshape

MD may be used to estimate quality and uniformity of polymerization as a function of shape and size of the feature. While reverse tone and/or DNR have been proposed as a potential solution to shape retention challenges, resist formulation can also be optimized for shape retention based on this investigation, if tone inversion is not desirable. It is hypothesized that the polymerization of the nanoshape is worse than the bulk due to shape and size influence. Polymerization is a spatial phenomenon and the probability of bond formation at a point in the nanoshape is a function of the amount of material surrounding the point within a certain radius. In bulk resist, this probability is constant except for local

stochastic variations. On the other hand, in a nanoshape, this probability is a function of both size and shape.

This phenomenon was studied by performing polymerization (using the MD framework) of the diamond & cross nanoshapes with various sizes starting from 25 nm and going down to 5nm and calculating the following parameters percentage polymerization as a function of size and shape.

Table 5 and Figures 32, 33 below shows the results after simulation and data analysis.

Nanoshape Size (nm)	Polymerization Percentage	
	Diamond	Cross
25	73	-
22.5	72	72
20	72	73
17.5	72	72
15.0	71	71
12.5	69	69
10.0	66	66
7.5	66	63
5.0	66	57
bulk	79	79

Table 5: Percentage polymerization as a function of nanoshape

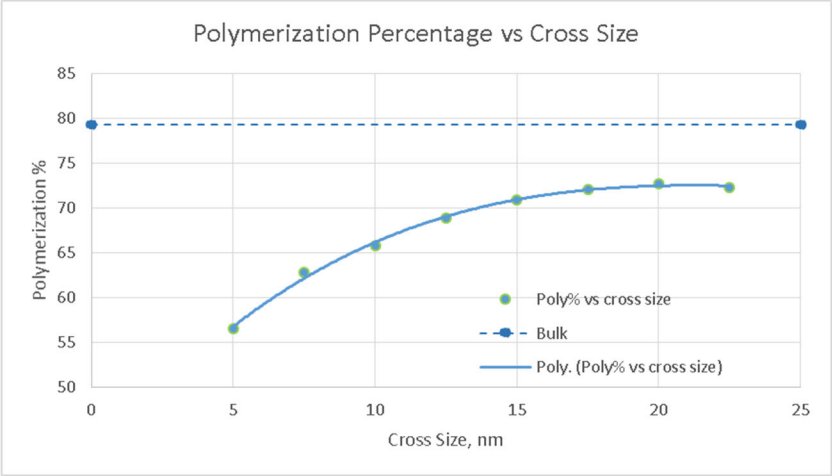

Figure 32: Percentage Polymerization versus Cross size

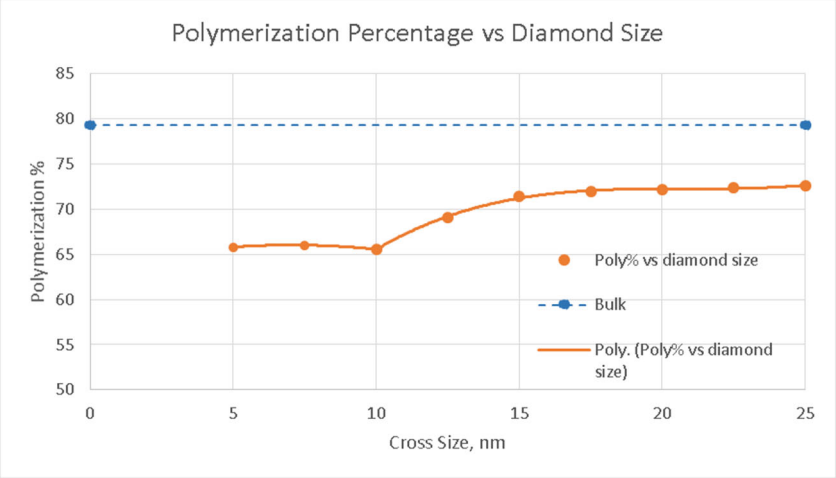

Figure 33: Percentage Polymerization versus Diamond size

The polymerization quality degrades with reducing nanoshape size and does not reach bulk polymerization value (79%) even for the largest nanoshape sizes. Further, the cross and diamond polymerization curves are not identical, especially below 10nm. This clearly shows the nanoshape size and shape adversely affect bonding below 25nm. It should be noted here that the bulk polymerization value reported here (79%) is different from value

reported earlier (~87%). This is due to a decision made to limit the bonding time for computational cost reasons.

Nanoshape effect on bonding efficiency

The spatial distribution of the un-polymerized double bonds was studied for the 25nm diamond and cross. The initial and final carbon double bond locations are shown in Figures 34 and 36 respectively. The bonds are binned in 20A square bins before and after polymerization (2D histogram in X-Y plane). The percentage polymerization can then be calculated for each bin and gives the spatial distribution of polymerization. Figures 35 and 37 show the local polymerization efficiency.

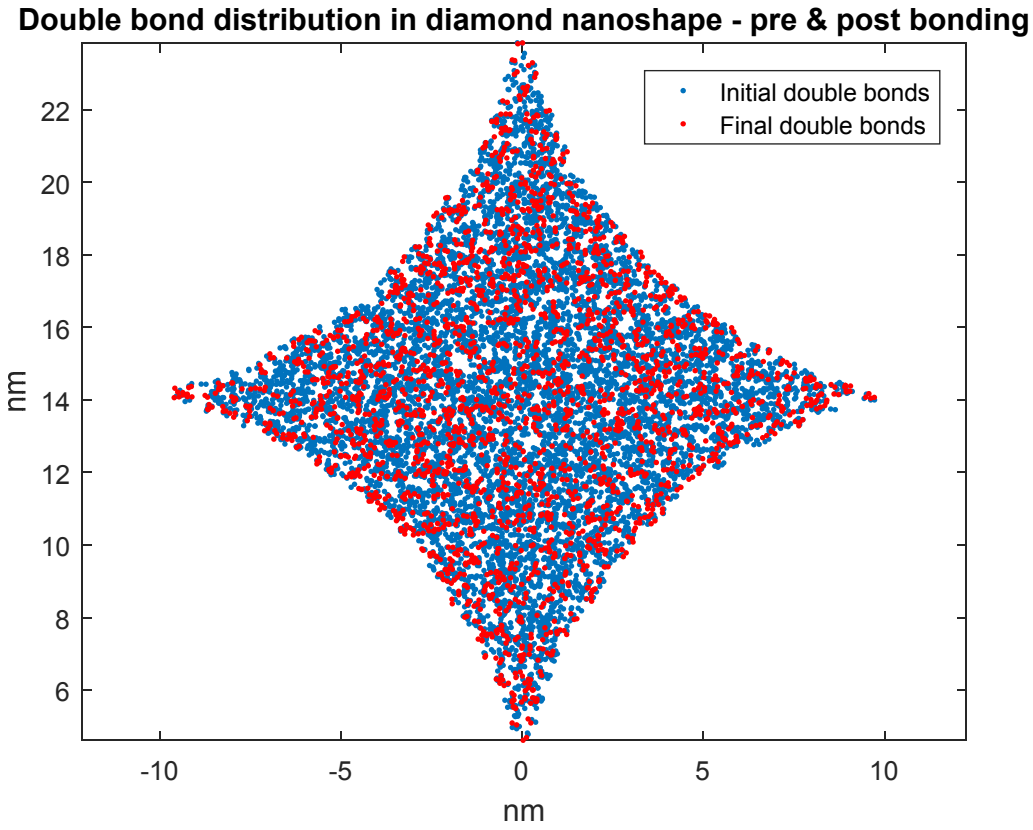

Figure 34: Double bonded carbon atom distribution before and after bonding

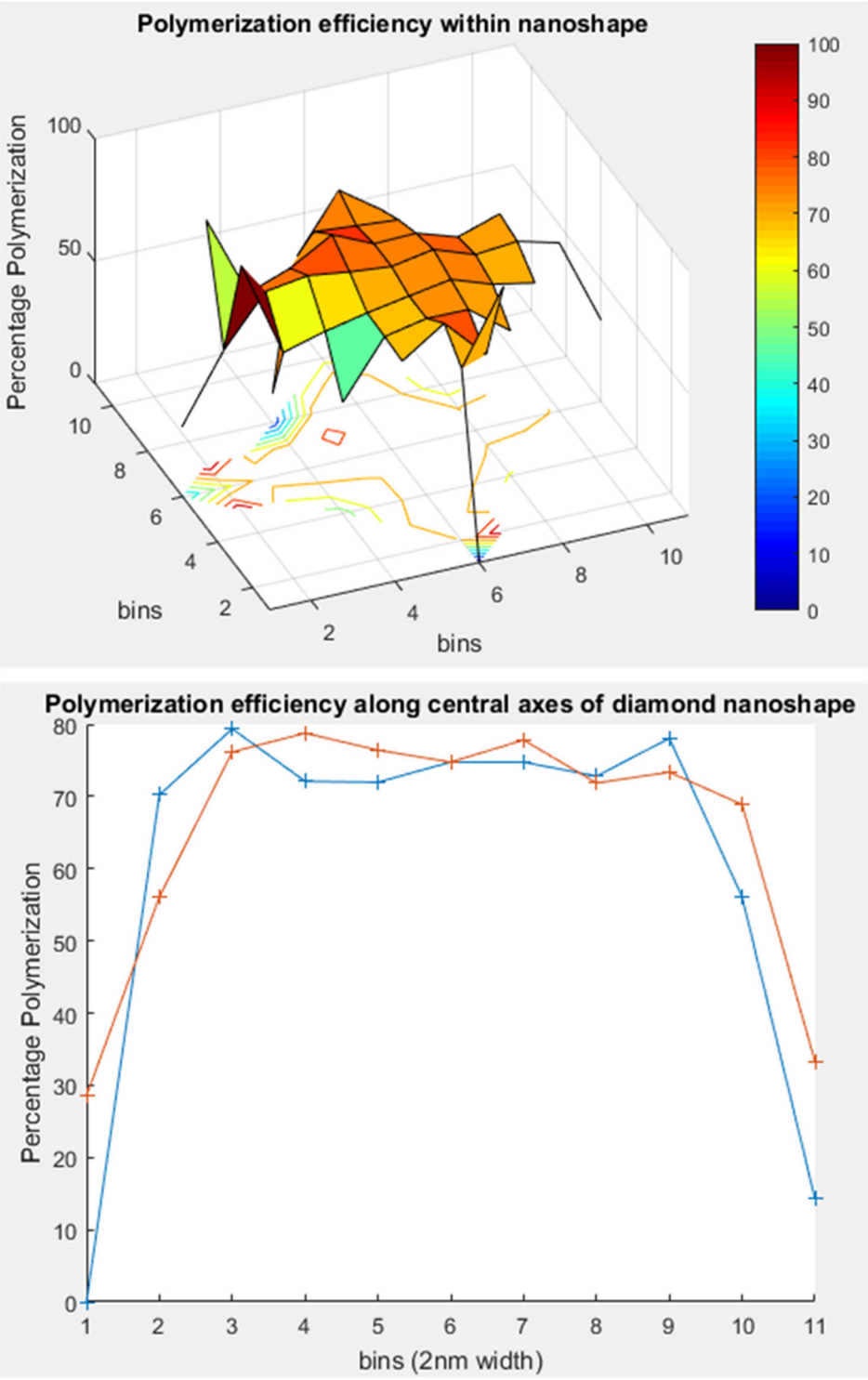

Figure 35: Polymerization efficiency within the diamond nanoshape, along the central axes

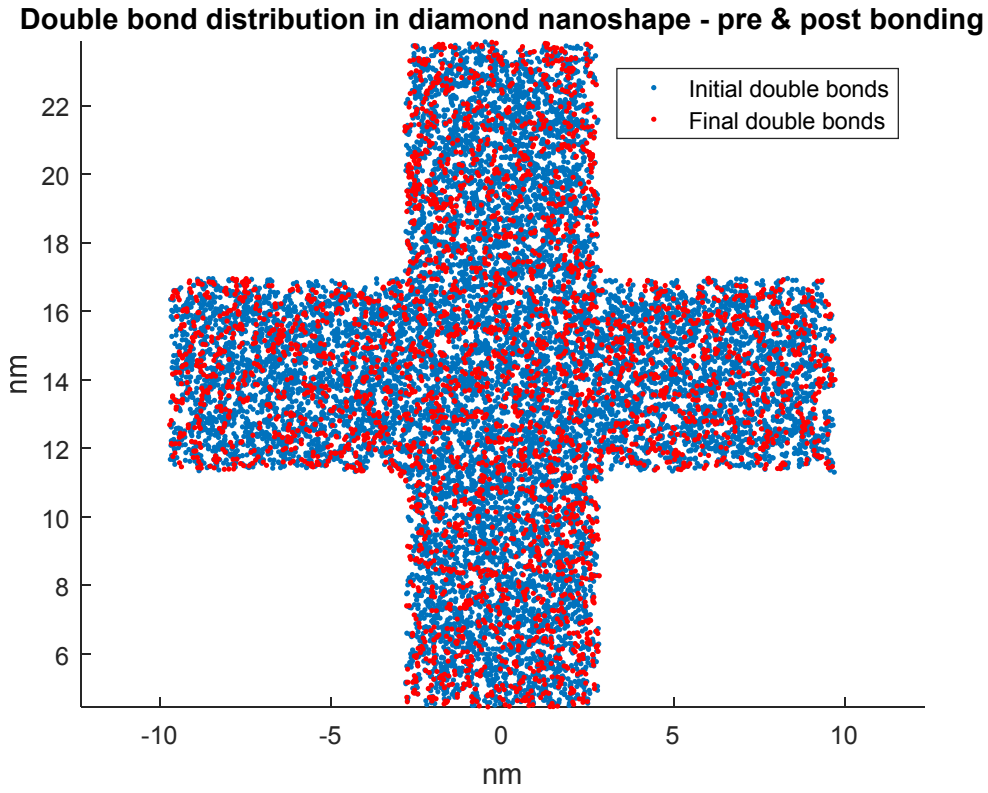

Figure 36: Double bonded carbon atom distribution before and after bonding

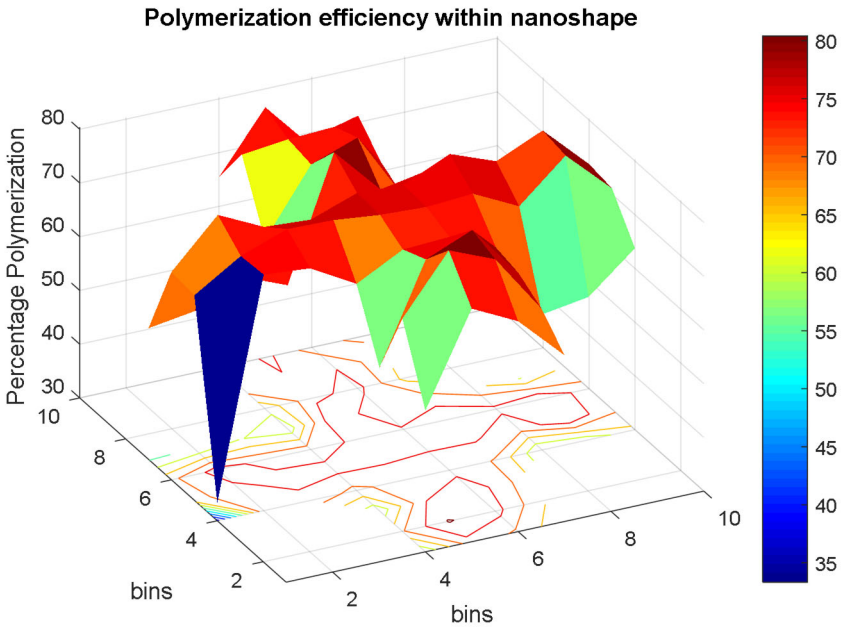

Figure 37: Percentage Polymerization versus Diamond size

As can be seen, there is a strong dependence of polymerization on the location within the nanoshape. In the diamond shape, the polymerization is similar to bulk (~80%) near the center of the feature and sharply degrades at the corners (~30-60%).

In the diamond shape also, the polymerization remains close to bulk along the middle axes of the feature and drops off on either side of the axes towards the edge and corners.

This kind of intra-feature bonding quality information could be used to predict which shapes are difficult to achieve and require tone inversion or DNR techniques developed earlier.

Computational Resist Design for Nanoshapes

An important design parameter that has not been explored thus far is the composition of the imprint resist. In this section, the MD framework is used to inform the resist formulation itself.

As discussed in Chapter 3, the resist composition taken from the literature consists of three acrylate molecules namely, hexyl acrylate (~55% w/w), isobornyl acrylate (~25% w/w) and ethylene glycol diacrylate (~20% w/w) as the cross linker (Figure 37).

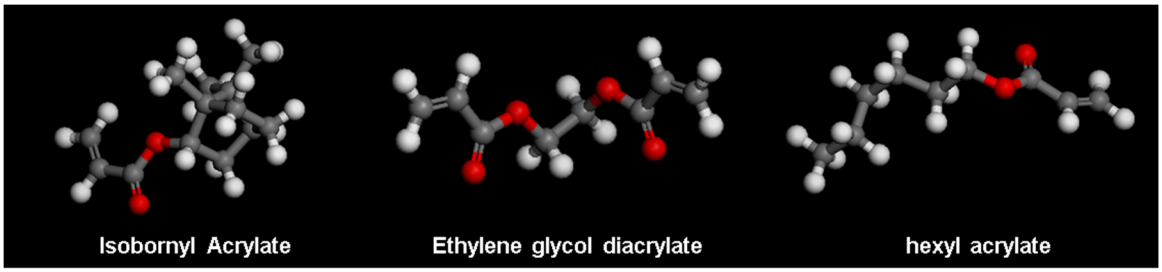

Figure 38: Imprint resist components.

MD by virtue of its versatility allows for investigation of various resist material formulations purely in-silico. It is proposed to leverage this computational material design capability to optimize imprint resist formulation specifically for shape retention in nanoshapes.

More specifically, based on crosslinking studies done with imprint resist [37], there is a correlation between crosslinker percentage in resist and the percentage polymerization. Higher crosslinker amounts lead to faster polymerization but reduce the percentage polymerization. These earlier studies were done for bulk resist material. It is unknown how crosslinker percentage impacts polymerization in nanoshapes. It is proposed to use the MD design tool at our disposal to study the effect of crosslinker on polymerization in cross and diamond shapes.

For this study, the cross nanoshape size is chosen and two new resist formulation are created with 10% and 40% crosslinker. Polymerization is simulated with each new resist formulation to analyze the effect on percentage polymerization. Figure 39 summarize the

results of this analysis. As can be seen, the effect of formulation change on polymerization roughly follows bulk resist behavior. For example, at the 10nm dimension, the percentage increases from 66 to 72% with the new formulation. The increased crosslinker density helps with bonding efficiency by about 10%. This resist material design parameter for improving nanoshape retention has been examined here in an exploratory way. This exercise should be repeated for each new nanoshape design consideration.

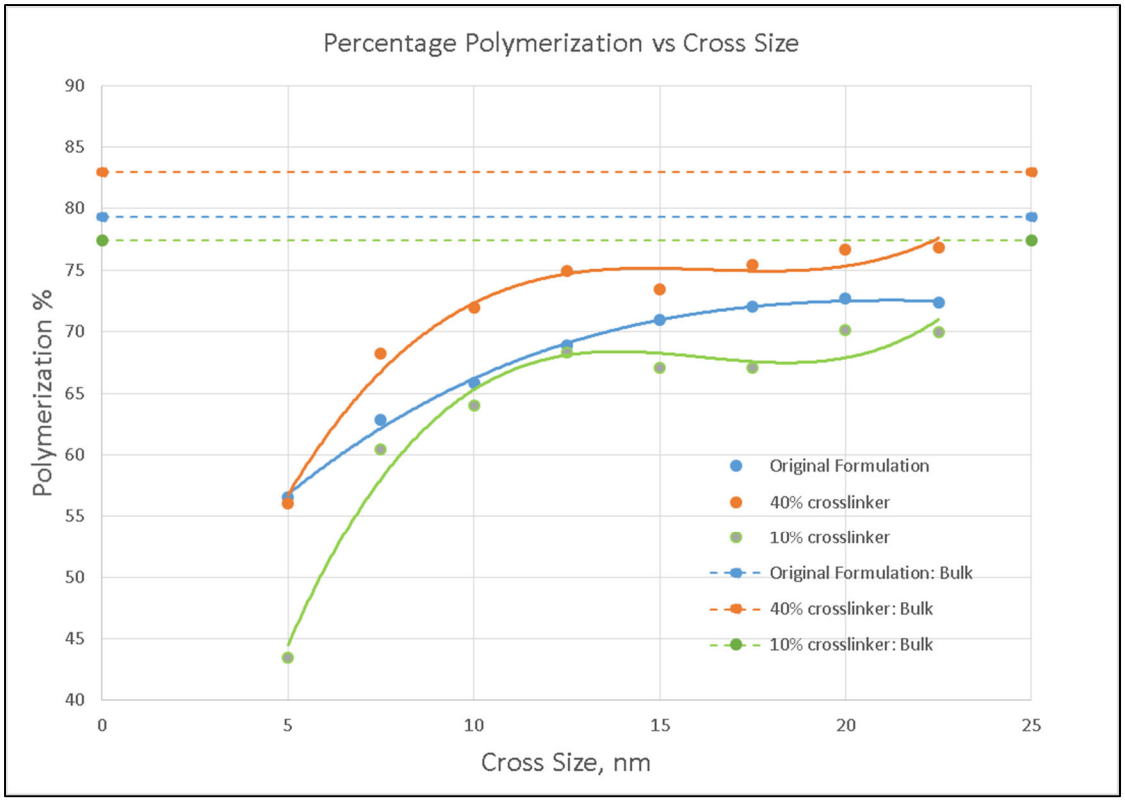

Figure 39: Polymerization as a function of crosslinker and cross size

Note that all material properties like modulus, strength and T_g will have to be re-estimated for the new formulation(s) to ensure performance in addition to increased cross-linking.

IMPROVING NANOSHAPE RETENTION USING RIE

The previous section showed that bonding becomes progressively poorer near the edges and sharp features of nanoshapes. RIE based DNR has been discussed earlier in the context of the creating a sharp corner in 200nm diamond fabrication. For smaller features also, a similar idea can be used but in this case the help the structural integrity of the nanoshape.

Figures 40 & 42 show a 10nm diamond and cross nanoshape respectively with a 2nm wide bridge on all four sides, retaining its original geometry significantly better than an isolated nanoshape (refer to Figures 29 and 30a). The bridge section of the feature maybe removed post imprint replication by designing a slightly isotropic etch chemistry. The target shape of the nanoshape after the etch is shown by the red dotted lines. The feature on the other side of the bridge could be the neighboring nanoshape structure or a dummy feature (in case of a different pitch requirement).

Figure 41 shows the bonding efficiency of an isolated diamond (same as Figure 35) compared to that of a bridged diamond. The bridged diamond shows significantly better bonding across the entire central axis thus confirming the structural integrity seen in the relaxation simulation.

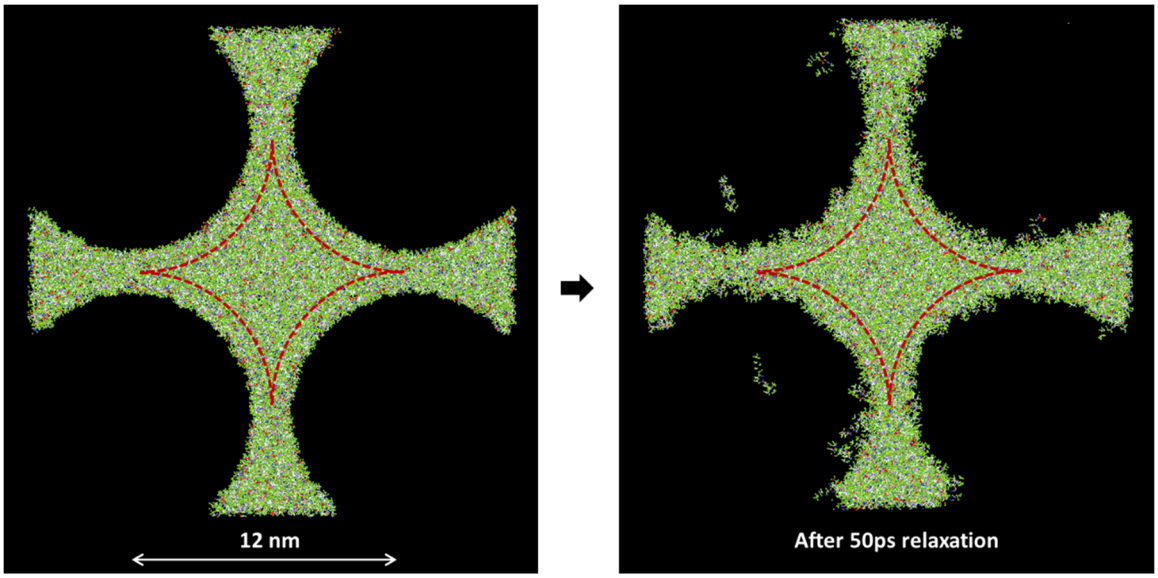

Figure 40: DNR to Overcome Bonding Inefficiency in diamond nanoshape.

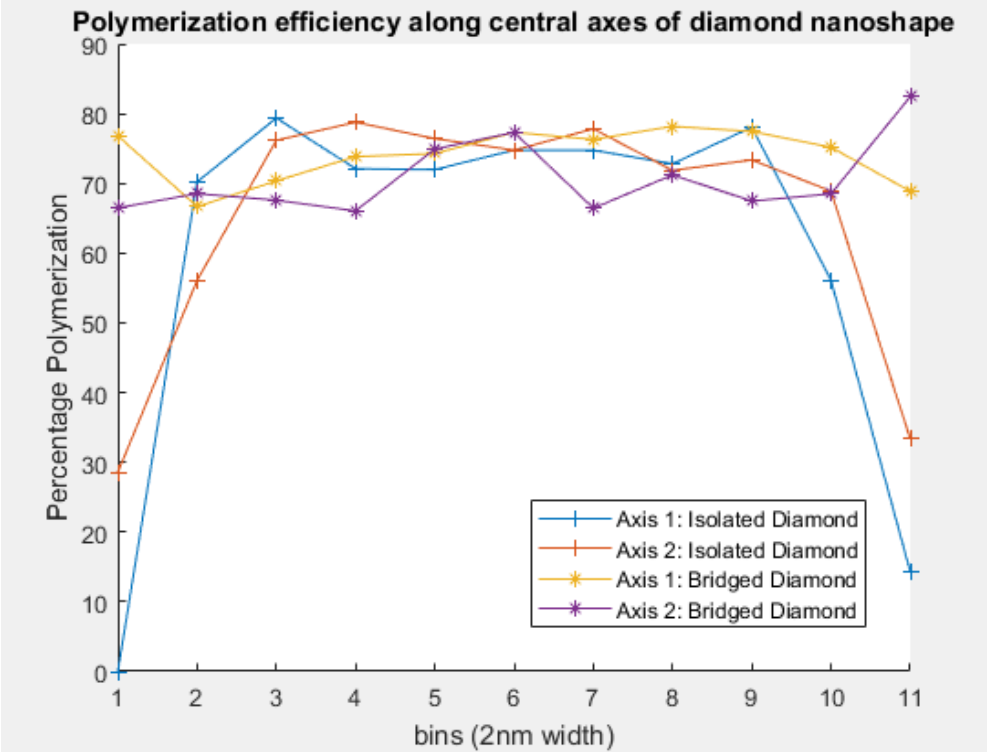

Figure 41: Polymerization efficiency within the diamond nanoshape, along the central axes

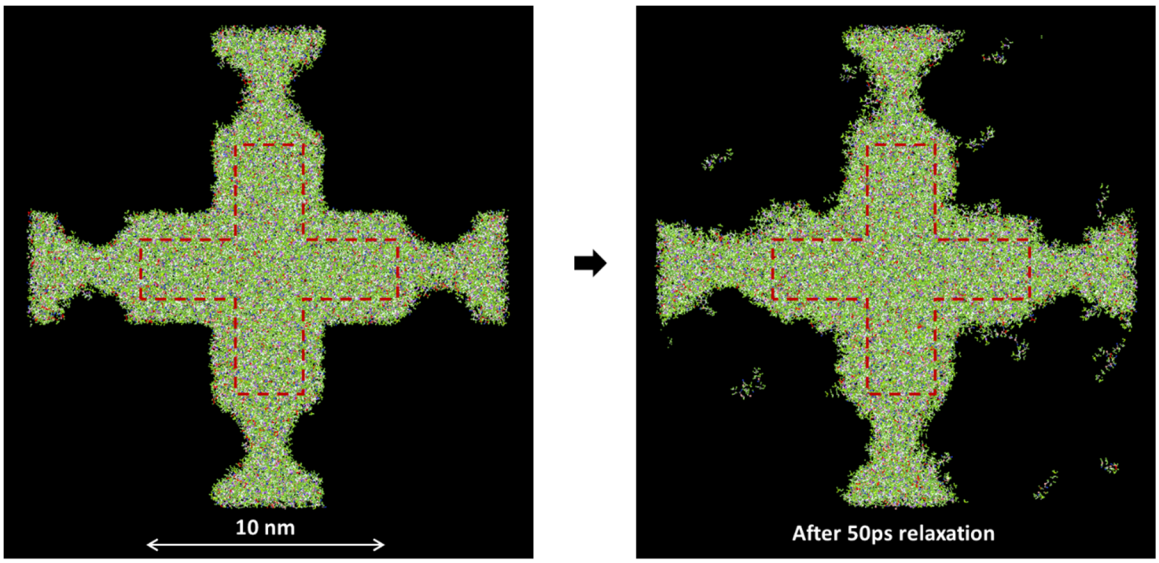

Figure 42: DNR to Overcome Bonding Inefficiency in cross nanoshape

EFFECT OF RESIDUAL LAYER THICKNESS (RLT)

In all the previous simulations, an infinitely long feature (periodic b.c. in the direction perpendicular to the plane of the figures) is assumed to isolate the in-plane behaviors. The actual fabricated nanoshapes will however have finite height and a residual layer (RLT) under the feature due to the nature of the J-FIL imprinting process. The effect of RLT on nanoshapes thus is an important consideration. The cross nanoshape structure(10x2.5nm) was simulated with an RLT in hole tone and allowed to relax for 50ps. Figures 43 & 44 show the resist behavior at the base of the cross hole nanoshape at a vertical cross-section through the middle of the feature respectively.

The nanoshape retention is generally similar to cross hole with periodic b.c (refer Figure 30).

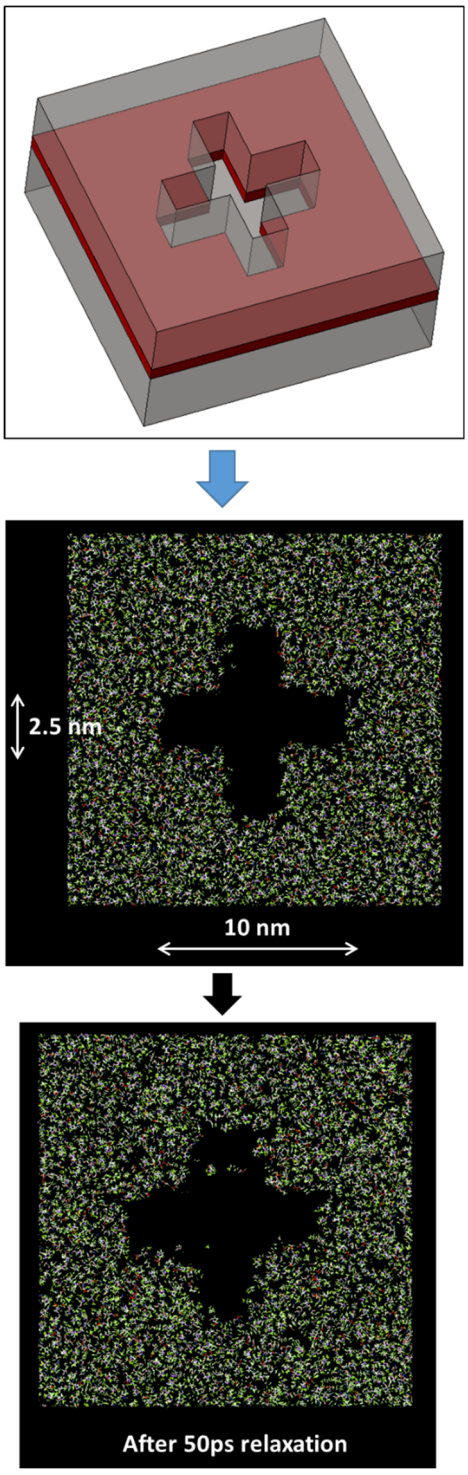

Figure 43: 10nm thick cross section at the base of the cross hole nanoshape shown schematically in red (top) and the MD model before and after relaxation

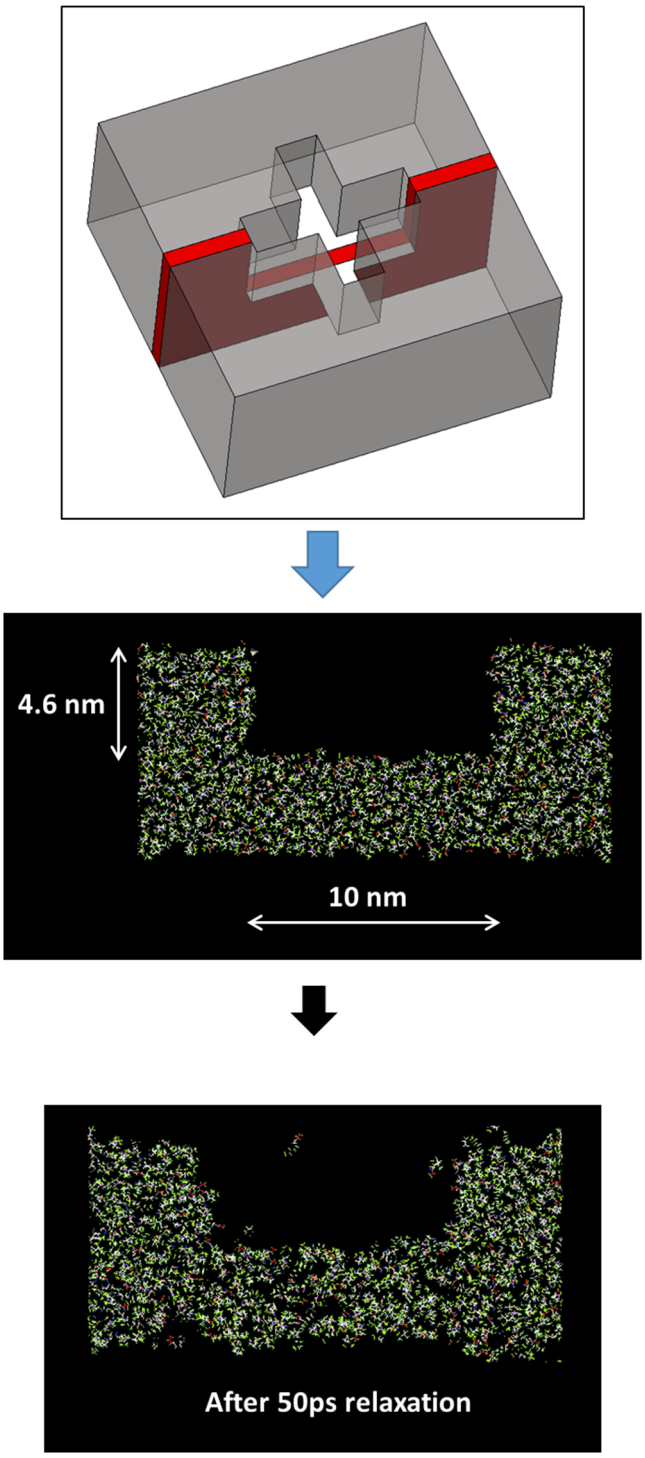

Figure 44: 10nm thick cross section at the base of the cross hole nanoshape shown schematically in red (top) and the MD model before and after relaxation

TEMPLATE DESIGN & FABRICATION FOR NANOSHAPES

In addition to the ALD based fabrication of nanoshape template, discussed earlier and new method for complex nanoshape template was explored. This method pioneered by Zyvex Corp., involves using STM (scanning-tunneling microscope) tips to selectively remove hydrogen atoms from a monolayer of hydrogen deposited on Silicon substrates [42].

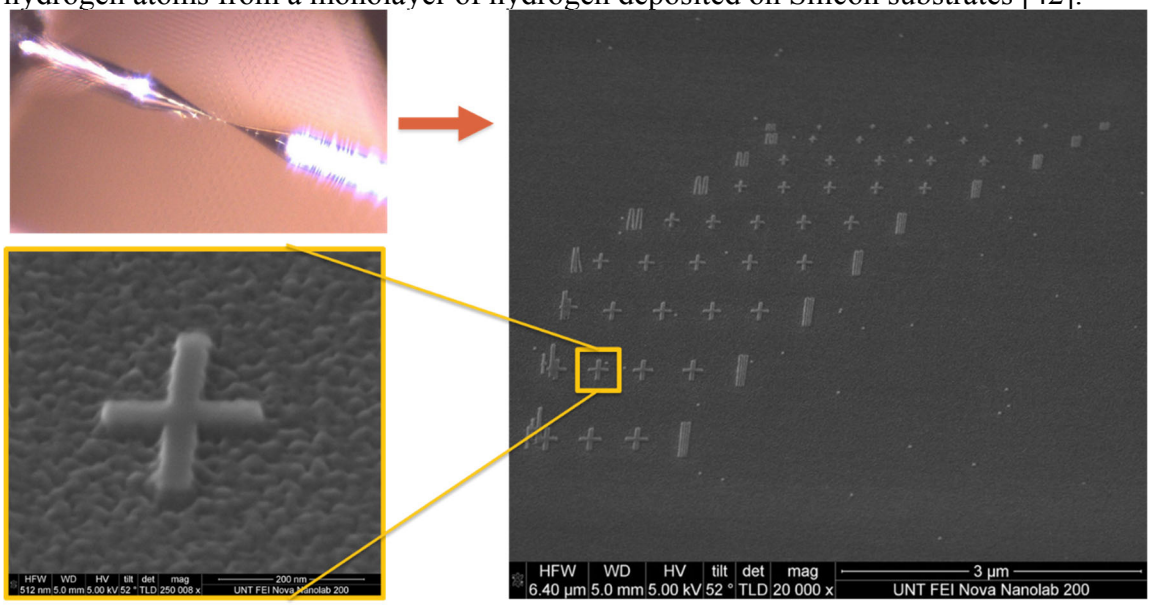

Figure 45: STM tip-based fabrication of cross nanoshape array in Silicon

The exposed silicon surface acts as a mask for further processing steps including ALD and dry etch to create the desired shaped structures. Zyvex was successfully able to fabricate an array of nanoshaped crosses of different sizes in addition to other complex shapes. Imprint replication of these templates was pursued but with limited success. The reason for failure to replicate the silicon template to a larger glass substrate is due to contamination of the silicon templates during processing. Figure 45 shows SEM image of the fabricated cross arrays. The STM tip is also shown in the upper left inset.

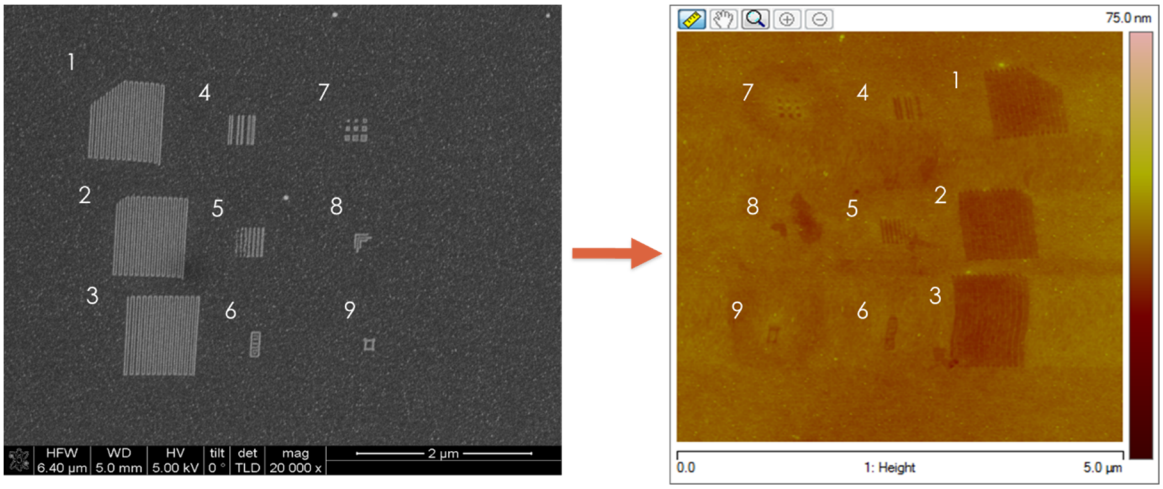

Figure 46: STM tip based fabricated template of various shapes (left) and AFM scan of imprint replication (right).

Figure 46 shows another silicon template with assorted shapes that was successfully replicated by imprinting. The imprinted resist was scanned by AFM and shows good shape retention. This early work shows existence proof of technology for nanoshape fabrication in the sub 25nm dimension range. Further work is needed to optimize the process flow to replicate from the STM written master template and fabricate large area nanoshape imprint templates.

Chapter 6: *Conclusions and Future Work*

CONCLUSIONS

In summary, the capability of imprint lithography to replicate nanoshaped structures was systematically studied by fabrication, modeling and metrology.

Nanoshaped diamond arrays were fabricated and an exemplary supercapacitor device was constructed with these features by deep etching and atomic layer deposition. The supercapacitor device exceeded conventional device performance by 90%, underscoring the basic premise of this work, namely that nanoshaped structures can enable a broad range of nanotechnology applications. STM tip based nanoshape templates were shown to be feasible and fabricated in collaboration with Zyvex Corp. This technology will be a primary source for master templates for sub 25nm nanoshapes.

A first principles atomic model of the imprint resist was developed and validated for material properties. A variety of nanoshape related simulations like nanoshape retention check, resist formulation, shape relaxation compensation and effect of RLT can now be performed without requiring any apriori material assumptions. The modeling efforts have established the following list of process variations to optimize nanoshape retention.

- Tone inversion
- Addition of sub-features
- Etch based compensation

In conclusion, nanoimprint lithography is uniquely suited for high volume nanoshaped structure fabrication and this work has created a fabrication and modeling framework to leverage this capability in a systematic and integrated manner. Two publications and one US patent have resulted in part from this work, namely references [1], [45] and [46].

FUTURE WORK

Contribution to DRAM Roadmap

DRAM (dynamic random access memory) is the work horse in modern computers. DRAM consists of a capacitor element which stores bit information namely 0s or 1s in the form of charge. The capacitor is connected to the so-called bit line and word lines by a pass transistor. By biasing the word line and bit line suitably, the capacitors can be charged and thus store information. Conversely, information can also be read from the capacitors by the bit and word lines. Figures 47 & 48 show the device roadmap of the three largest DRAM manufacturers and corresponding capacitor scaling challenges respectively [47].

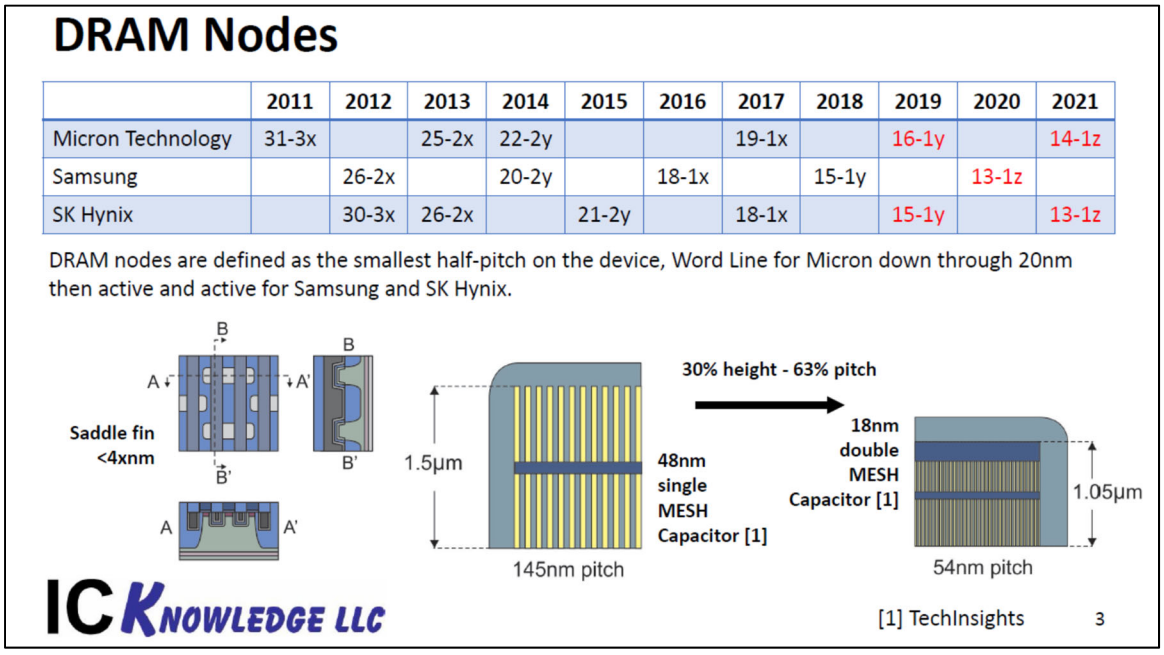

Figure 47: Device roadmap of the three largest DRAM manufacturers

The industry's effort to increase capacitance (~1.2 to 3.3X) is focused mainly on using high-k dielectric materials. However, it has already been demonstrated in this work that

~2X increase in capacitance is possible by nanoshaping the capacitor structure. Further, the MD modeling indicates scalability down to ~10nm diamond like feature sizes. These two results directly enable us to help the memory industry to achieve the DRAM roadmap and are therefore a key contribution of this work.

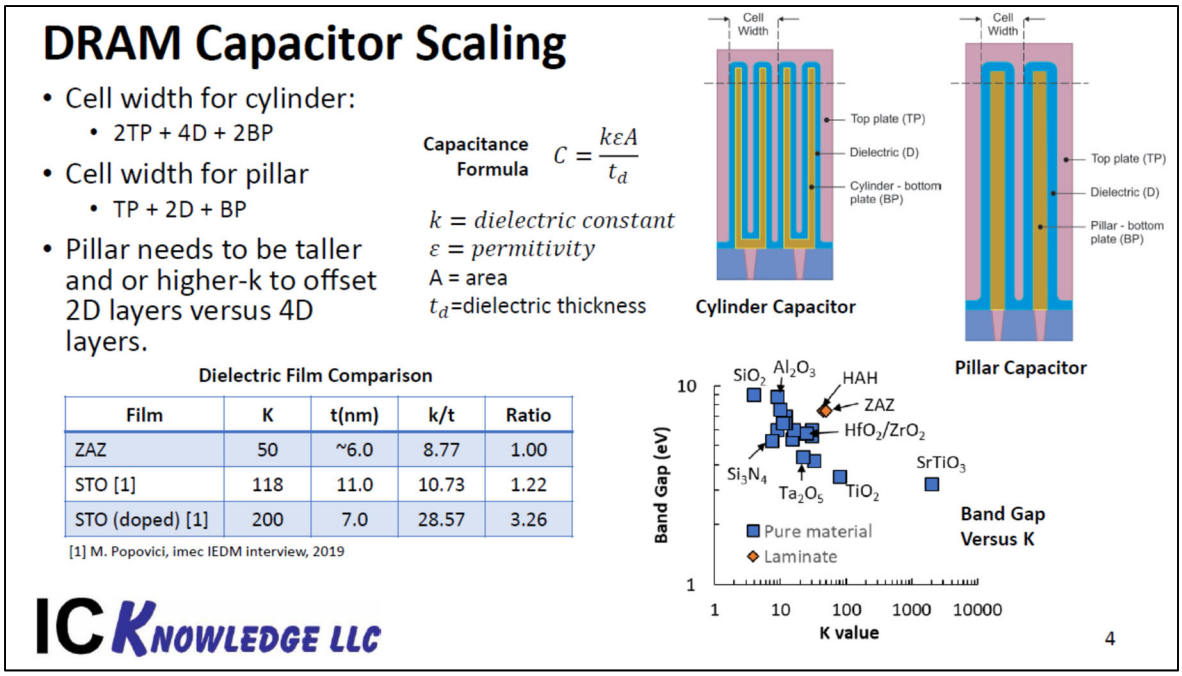

Figure 48: DRAM capacitor scaling challenges corresponding to the device roadmap

Multiscale Modeling

Several interesting concepts and directions are available as a continuation of the modeling work presented here. This section highlights some of the modeling and metrology ideas that can be explored by researchers in the future.

The present MD framework can be used as-is for the following interesting and important problems:

Nanoparticle damage to fused silica templates

Nanoscale resist flow and filling behavior in templates

Resist viscosity simulations

Separation behavior of small features

Size scaling and time scaling are obviously the two dominant limitations of molecular dynamics simulations. There is a voluminous body of literature on several continuum to atomic coupling methods as part of the multiscale modeling framework [43]. Finite element codes can be coupled with LAMMPS to pass force and atom/ node position information back and forth to run a coupled multiscale analysis [44]. Care must be taken to account for the so-called ghost forces that occur at the interface of any continuum-atom numerical computation scheme [43].

Model Reduction

In all the modeling work presented here, an all-atom MD model was used. Several so-called coarse-grained MD models are also commonly used in simulations. These involve lumping several atoms into a single mass thus reducing the number of particles in the system and thus reduce computational cost while introducing a model insufficiency. Coarse grained models should be carefully validated against experimental data. A systematic validation and uncertainty quantification scheme based on Bayesian methods is outlined next.

Validation and Uncertainty Quantification (VUQ)

Classical validation of MD models can be done with direct comparison of experimental data with the model. For example, nano-indentation experiments commonly yield nanoscale modulus information for polymers. This can be compared to the MD

results. Reduced models are also compared to fully resolved (all atom models in this case) MD models if computationally feasible.

The more rigorous general validation plan for a reduced MD model as described in the above sections is as follows.

In our case, the end goal is to generate a posterior distribution for observables ***y*** from the model that will then be compared to the experimental data. The equation for the posterior distributions is given by the equation 7 below.

$$p(y|D, X) = \int_{\tilde{y}} \int_{\theta} p(y|\tilde{y}, \theta, X) p(\tilde{y}|\theta, X) p(\theta|D, X) d\theta . d\tilde{y} \quad (7)$$

The model credibility can then be ascertained based on quartile or HPRD methods. The steps to obtain the above posterior distribution are detailed below.

1. Identify proposed use of MD model
2. Formulate the physical model for atomic interactions (The MD model)
3. Introduce model inadequacy in the force field (embedded theory part)
4. Formulate priors for the forcefield error terms
5. Calibration of the forcefield parameters
6. Calculation of likelihood integral
7. Calculation of posterior observables
8. Credibility calculation

Other analysis that will be useful include:

a) determining the domain of applicability of validated model. Specifically, identifying the parameters that the model inadequacy is sensitive to and,

b) cross model comparison, specifically comparing the validity of so called coarse grained MD models to see at which level of model reduction the model loses credibility.

A detailed description of the above items is as follows:

1. Identify proposed use of MD model

   The purpose of an MD model for polymer materials is to predict the material characteristics of structures made with these polymers in the nanoscale. So, in the context of the three applications for computational models discussed in class (predictions, data analysis, consequence of theories), this falls under the "making predictions" category.

2. Molecular dynamics is the science of applying Newton's laws of dynamics to individual atoms and molecules. The constitutive relationship is the interatomic forces between atoms. This is called the forcefield and is calculated from first principle quantum mechanical interactions between the atoms. The forcefield has several terms to account for interactions due to chemical bonds, Van der waal's forces, bond angles, bond torsions etc. The forcefield is designed to be as simple as possible while adequately describing the various interactions. This is because calculation of the force on each atom from the forcefield is computationally expensive. Therefore the forcefield is the embedded part of the dynamics. The time stepping is usually done by a Verlet integration to obtain new positions and

velocities. The initial velocities are assigned by sampling from a Gaussian distribution, the magnitudes depending on the model temperature.

3. A typical forcefield for organic molecules is the CFF series of fields. The force field has several parameters as shown in Figure 24., but the basic equation of motion for atom ***i*** is:

$$m_i a_i = F_i(r, q) \qquad (8)$$

Where,

m_i = mass of atom *i*

a_i = acceleration of atom *i*

F_i = force on atom *i* and is a function of:

vector ***r*** the position of all atoms at time ***t***,

vector ***q*** being the charge distribution in the atoms.

The relative bond angles θ_i are calculated from the ***r*** vector.

One approach in coarse graining, for example, to accommodate the removal of C-H bonds is to introduce probability distributions for all the parameters while eliminating the hydrogen atom terms from the forcefield. Another approach is to keep all the original non hydrogen parameters and introduce a separate term to compensate for the inadequacy. One reasonable model for this separate term stems from studying the Van der Waal's interaction between atoms. Since the hydrogen atom is considered to be stiffly attached to the carbon atom in our reduced model, it can only interact in a non-bonded way with neighboring atoms. This is like a Van der waal's interaction that is approximated by the so called Lennard Jones (LJ) potential. The LJ potential looks like:

$$V_{LJ} = 4\varepsilon\left[\left(\frac{\sigma}{r}\right)^{12} - \left(\frac{\sigma}{r}\right)^{6}\right] \quad (9)$$

Where **ε** and **σ** are parameters that need to be inferred from a Bayesian inference and **r** is distance between atom pairs. This formulation incorporates both attractive and repulsive forces and the $1/r^6$ drop off in the force which is typical of dipole - dipole interactions.

4. There are two prior distributions in this formulation, **ε** and **σ.** The **ε** term is a scaling factor and known to be positive. This can therefore be modeled as a Jeffrey's distribution for example. Another choice is a log-normal distribution. The mean value can be taken to be the LJ parameter for H-H pair interactions, $\boldsymbol{\varepsilon_{H\text{-}H}}$, from the literature. The standard deviation can be of the same order as $\boldsymbol{\varepsilon_{H\text{-}H}}$.

σ is also known to be positive and therefore can be modeled similar to **ε** with a lognormal distribution, the mean and standard deviation of which can be taken from H-H pair data from the literature.

In summary the equation of motion for atom ***i*** changes to:

$$m_i a_i = F_i(r, q) + F_m(r, \varepsilon, \sigma) \quad (10)$$

Where, $F_m = 4\varepsilon\left[\left(\frac{\sigma}{r}\right)^{12} - \left(\frac{\sigma}{r}\right)^{6}\right]$, and ε, σ are log-normal or Jeffrey's distributions explained above. This formulation will be required for each atom type in the model. In the

PMMA case, there are at least 3 atoms types, Carbon, Hydrogen and Oxygen. Double bonded carbon is sometimes treated separately from single bonded carbon.

5. Calibration and inference can be done with say experimental data from a nanoindentation experiment or with pattern geometry information from an scanning electron microscope (SEM). The error models of these instruments would be required to formulate the likelihood. For example, it is known that the accuracy of SEM machine is around 0.5nm. This can be taken as the standard deviation of the error model, with the mean being the measurement value.

6. It should be noted that the MD model is treated as probabilistic and not deterministic. The reason for this is that the initial velocities are chosen randomly from a gaussian distribution and will therefore lead to different velocities and positions at the end of the each new MD run. This, along with numerical error will give a distribution of model outputs rather than one single value. The likelihood is therefore given by:

$$L(\theta, \varphi; \tilde{y}) = p(\tilde{y}|\theta, \varphi, X) = \int_y \underbrace{p(\tilde{y}|y, \varphi, X)}. \underbrace{p(y|\theta, X)dy} \qquad (11)$$

Measurement error model for SEM or nanoindentation

Probabilistic MD model

The first term in the integral is a standard measurement error model. The second term is a probabilistic model of the MD model and is interpreted as follows. Given the prior distributions in our case, we have two priors for each atom type for a total of six priors. An

MCMC algorithm samples **θ** from these distributions and feeds it as input to the MD model given in equation 2. The MD model will have to be run a number of times for each prior sample to generate samples of the second term above. The likelihood is then numerically integrated with this sampling.

The posterior distribution of the parameters is then obtained by a Bayesian update.

$$p(\theta|\mathrm{D},\mathrm{X}) \propto \mathrm{L}(\theta,\varphi,\mathrm{X}).\mathrm{p}(\theta|X) \quad (12)$$

7. The calculation of the posterior distribution of observables is then given by:

$$\mathrm{p}(\mathrm{y}\,|\mathrm{D},\,\mathrm{X}) = \int_{\tilde{y}} \int_{\theta} p(y|\tilde{y},\theta,X)p(\tilde{y}|\theta,X)p(\theta|D,X)d\theta.\,d\tilde{y} \quad (13)$$

The last term is the MCMC samples of the parameters generated in step 6. The middle term is the MD model. These samples are also available from step 6 above. The first term is the measurement error model generated over a grid of points in the expected observables range.

8. The credibility calculations can be performed to obtain α values for the experiment data compared to posterior distribution above. The order of magnitude of α is important. For example α = 1e-5 would invalidate the model vs α = 0.4 ,say, would be a data point validating the model.

Once the above frame work is in place, different coarse grained models can be compared and validated or invalidated.

As far as domain of applicability, temperature would probably play a major role. This is because, polymer properties change dramatically with temperature especially near the so called glass transition temperature T_g, where the polymer becomes visco-elastic and rubbery above T_g and remains much more stiffer and "plastic" like below T_g.

Also, any changes in composition of PMMA such as addition of ionic materials or more generally presence of electromagnetic fields will probably change the distributions of ε and σ significantly and invalidate the model. This is because the parameters are Van der waal's terms assumed to work in space free of electromagnetic fields.

In summary, a general scheme to introduce forcefield inadequacy for simplification of computational MD models is explored. The inadequacy is modeled as a Lennard Jones potential with distributions for the LJ parameters. Two parameters will be inferred for each atom type in the model. Since the physical model is a MD model, this VUQ exercise could be computationally expensive and hence the MD system chosen should be as small as possible. For example, a single molecule system can be used to match the experimental vibration spectrum to the spectrum estimated from the reduced MD model. Also, calculation of likelihood involves evaluation of high dimensional integral. A VUQ framework would nonetheless be very valuable for validating and comparing coarse grained MD models for use in nanofabrication predictions.

AFM Metrology for bonding efficiency estimation

Advanced AFM scanning techniques using infra-red radiation signatures can detect atomic vibration spectra on samples. This can be used, for example, to probe a nanoshape spatially for carbon-carbon double bond density variations within the nanoshape to validate

the MD simulation results. Figure 49 shows an example application that differentiates between polystyrene and polymethylmethacrylate phases in a sample based on the carbon-oxygen double bond resonance frequency.

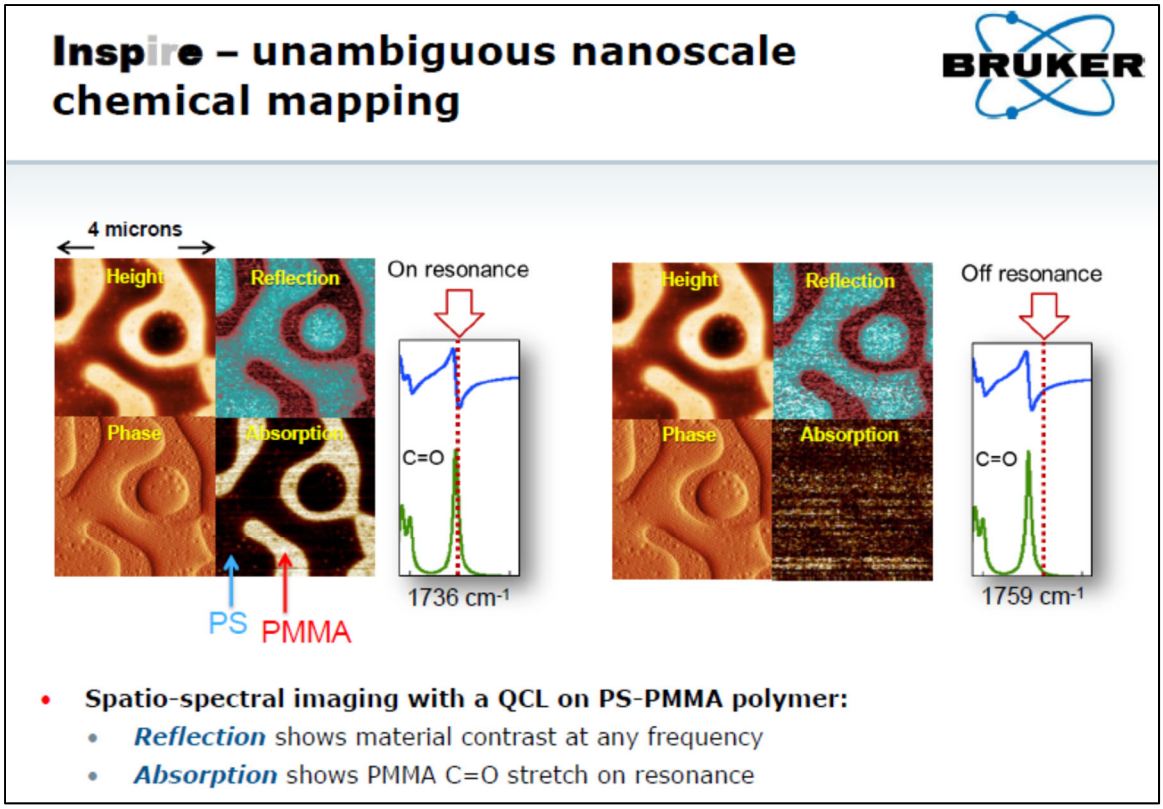

Figure 49: Advanced IR-AFM methods used to chemically differentiate the sample based on response at particular resonant frequencies. Source: www.bruker.com

AFM based Nanoindentation & simulation

Similarly, AFM based nanoindentation methods can be used to probe for local material properties like modulus and poisson's ratio with ~10nm resolution (Figure 50). This metrology is highly applicable for measuring property variation within the nanoshapes.

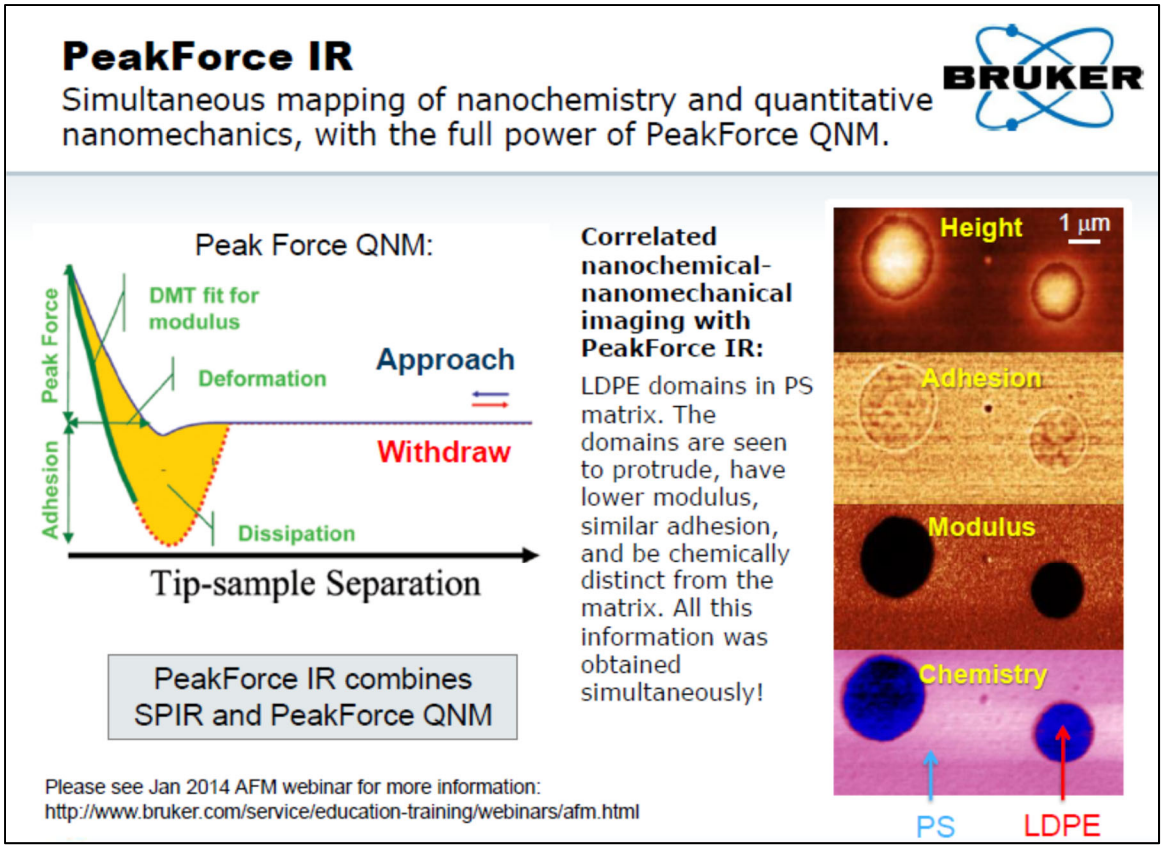

Figure 50: Advanced QNM-AFM methods used to differentiate the sample based on local modulus estimation by nanoindentation response. Source: www.bruker.com

Nanoindentation simulations can be performed in MD on nanoshape features and used to cross-correlate results from AFM and further to validate MD models.

References

[1] A. Cherala, M. Chopra, B. Yin, A. Mallavarapu, S. Singhal, O. Abed, R. Bonnecaze, S.V Sreenivasan, "Nanoshape Imprint Lithography for Fabrication of Nanowire Ultra-capacitors", IEEE Transactions on Nanotechnology, vol. 15, Issue 3, pp 448-456, May 2016.

[2] J. Lu and J. Vuckovic, "Nanophotonic Computational Design," Optics Express, vol. 21, Issue 11, pp. 13351-13367, Jun. 2013.

[3] S. Cakmakyapan, N. Cinel, A. Cakmak, E. Ozbay, "Validation of electromagnetic field enhancement in near-infrared through Sierpinski fractal nanoantennas", Optics Express, vol. 22, Issue 16, pp. 19504--19512, Aug. 2014.

[4] T. Pramanik, U. Roy, M. Tsoi, L. Register, S. Banerjee, "Micromagnetic simulations of spin-wave normal modes and the spin-transfer-torque driven magnetization dynamics of a ferromagnetic cross", Journal of Applied Physics 115, 17D123 (2014); doi: 10.1063/1.4863384.

[5] B. C. Stipe, T. C. Strand, C. C. Poon, H. Balamane, T. D. Boone, J. A. Katine, J. Li, V. Rawat, H. Nemoto, A. Hirotsune, O. Hellwig, R. Ruiz, E. Dobisz, D. S. Kercher, N. Robertson, T. R. Albrecht, and B. D. Terris, "Magnetic Recording at 1.5 Pb m-2 Using an Integrated Plasmonic Antenna," Nature Photonics, vol. 4, Issue 7, pp. 484-488, Jul. 2010.

[6] R. Agarwal, V. Singh, P. Jurney, L. Shi, S. V. Sreenivasan, and K. Roy, "Mammalian cells preferentially internalize hydrogel nanodiscs over nanorods and use shape-specific

uptake mechanisms," Proc. of the National Academy of Sciences of the United States of America, vol. 110, No. 43, pp. 17247-17252, Oct. 2013.

[7] S. J. Lam, N. M. O'Brien-Simpson, N. Pantarat, A. Sulistio, E. H. H. Wong, Y. Chen, J. C. Lenzo, J. A. Holden, A. Blencowe, E. C. Reynolds, G. G. Qiao. "Combating multidrug-resistant Gram-negative bacteria with structurally nanoengineered antimicrobial peptide polymers", Nature Microbiology, vol 1, Article 16162, Sep. 2016.

[8] L. Harriott, "Limits of Lithography", Proceedings of the IEEE, vol. 89, No. 3, pp. 366-374, Mar. 2001.

[9] J. Bruning, Optical Lithography… 40 years and holding, Proceedings of SPIE Microlithography, 2007.

[10] L. Lattard, M. McCallum, R. Morton, T. Fujiwara, K. Makino, A. Tokui, N. Takahashi, and S. Sasamoto, "Spacer process and alignment assessment for SADP," Proceedings of SPIE Advanced Lithography, vol. 8326, Paper No. 8326-03, Feb. 2012.

[11] F. Hua, Y. Sun, A. Gaur, M. A. Meitl, L. Bilhaut, L. Rotkina, J. Wang, P. Geil, M. Shim, and J. A. Rogers, "Polymer Imprint Lithography with Molecular-Scale Resolution," Nano Letters, vol. 4, No.12, pp. 2467-2471, Dec. 2004.

[12] S.Y. Chou, P. R. Krauss, and P. J. Renstrom, "Nanoimprint Lithography," Science vol. 272, No. 5258, pp. 85-87, Apr. 1996.

[13] S.Y. Chou, C. Keimel, and J. Gu, "Ultrafast and direct imprint of nanostructures in silicon," Nature vol. 417, No. 6891, pp. 835-837, Jun. 2002.

[14] M. D. Austin, H. Ge, W. Wu, M. Li, Z. Yu, D. Wasserman, S. A. Lyon, and S. Y. Chou, "Fabrication of 5 nm linewidth and 14 nm pitch features by nanoimprint lithography," Applied Physics Letters, vol. 84, Issue 26, pp. 5299-5301, Jun. 2004.

[15] S.V. Sreenivasan, "Nanoimprint Lithography Steppers for Volume Fabrication of Leading-Edge Semiconductor Integrated Circuits," Microsystems and Nanoengineering, To Appear, 2017.

[16] S.V. Sreenivasan, "Nanoscale Manufacturing Enabled by Imprint Lithography," MRS Bulletin, vol. 33, Issue 9, pp. 854-863, Sep. 2008.

[17] http://semiengineering.com/why-euv-is-so-difficult/

[18] McCord, M.A., et al., "REBL: Design progress toward 16nm half-pitch electron-beam lithography," Proc. of SPIE Advanced Litho., Vol. 8323, Alternative Lithographic Tech. IV, Paper No. 8323-36, San Jose, CA, February 2012.

[19] Slot, E.; Wieland, M. J.; et al., "MAPPER: High Throughput Maskless Electron Beam Lithography," Emerging Lithographic Technologies XII. Edited by Schellenberg, Frank M., Proceedings of the SPIE, Volume 6921, pp. 69211P-69211P-9 (2008).

[20] C. A. Ross, et al., "Si-containing block copolymers for self-assembled nanolithography," J. Vac. Sci. Technol. B, 26, 2489 (2008).

[21] M. Harumoto et al., "Investigation of coat-develop track system for placement error of contact hole shrink process," Proc. SPIE 9777, Alternative Lithographic Technologies VIII, 97770O (April 1, 2016); doi:10.1117/12.2219925

[22] Ren, J., et al., “Engineering the kinetics of DSA toward fast dynamics and low defectivity,” Emerging Patterning Technologies,
Proceedings of SPIE Advanced Lithography, San Jose, CA, February 2017.

[23] J. Randall, J. Von Ehr, J. Ballard, J. Owen, R. Saini, E.Fuchs, H. Xu, S. Chen, “Atomically Precise Manufacturing: The Opportunity, Challenges, and Impact”, Atomic Scale Interconnection Machines, Springer, 2012.

[24] D. J. Resnick, W. J. Dauksher, D. P. Mancini, K. J. Nordquist, E. S. Ainley, K. A. Gehoski, J. H. Baker, T. C. Bailey, B. J. Choi, S. C. Johnson, S. V. Sreenivasan, J. G. Ekerdt, and C. G. Willson, “High-resolution templates for step and flash imprint lithography,” Proceedings of SPIE vol. 4688, pp. 205-213, Jul. 2002.

[25] S. M. George, “Atomic Layer Deposition: An Overview,” Chem. Rev., vol. 110, no. 1, pp. 111–131, Jan. 2009.

[26] K. Yoshimoto, T. S. Jain, K. Van Workum, P. F. Nealey, and J. J. de Pablo, “Mechanical heterogeneities in model polymer glasses at small length scales,” Physical Review Letters, vol. 93, No. 17, pp. 175501-1 – 175501-4, Oct. 2004.

[27] Z. Huang, N. Geyer, P. Werner, J. de Boor, and U. Gösele, “Metal-assisted chemical etching of silicon: A review,” *Advanced Materials,* vol. 23, Issue 2, 285-308, Jan. 2011.

[28] J. D. Plummer, M. D. Deal, and P. B. Griffin, “Thermal Oxidation and the Si/SiO2 Interface,” in Silicon VLSI Technology—Fundamentals Practice and Modeling. Englewood Cliffs, NJ: Prentice-Hall, 2000, pp. 301-311.

[29] Y. Zhai, M. Palard, L. Mathew, M. M. Hussain, G. C. Grant Willson, E. Tutuc, and S. K. Banerjee, "Fabrication of three-dimensional MIS nano-capacitor based on nanoimprinted single crystal silicon nanowire arrays," Micro and Nanosystems, vol. 4, No. 4, pp. 333-338, Dec. 2012.

[30] P. Banerjee, I. Perez, L. Henn-Lecordier, S. B. Lee, and G. W. Rubloff, "Nanotubular metal–insulator–metal capacitor arrays for energy storage," Nature Nanotechnology, vol. 4, No. 5, pp. 292-296, Mar. 2009.

[31] M. Steinhauser, "Computational Multiscale Modeling of Fluids and Solids: Theory and Applications", Springer Publications, 2008.

[32] R. L. Burns, S. C. Johnson, G. M. Schmid, E. K. Kim, M. D. Dickey, J. Meiring, S. D. Burns, N. A. Stacey, C. G. Willson, D. Convey, Y. Wei, P. Fejes, K. A. Gehoski, D. P. Mancini, K. J. Nordquist, W. J. Dauksher, and D. J. Resnick, "Mesoscale modeling for SFIL simulating polymerization kinetics and densification," Proceedings of SPIE, vol. 5374, pp. 348-360, May 2004.

[33] D. McQuarrie, J. Simon, "Molecular Thermodynamics", University Science Books, 1999.

[34] S. Plimpton, "Fast Parallel Algorithms for Short-Range Molecular Dynamics", Journal of Computational Physics, Issue 117, Issue 1, pp. 1-19, 1995.

[35] F. Xu, M. Watts, N. Stacey, "Materials for Imprint Lithography", US Patent 8,076,386, Dec 2011.

[36] Dauber-Osguthorpe, P.; Roberts, V. A.; Osguthorpe, D. J.; Wolff, J.; Genest, M.; Hagler, A. T. “Structure and energetics of ligand binding to proteins: E. coli dihydrofolate reductase-trimethoprim, a drug-receptor system"”, Proteins: Structure, Function and Genetics, Vol 4, Issue 1, pp. 31-47, 1988.

[37] G. Wiederrecht, “Handbook of Nanofabrication”, Ch 5, Elsevier Publications, 2010.

[38] F. H. Stillinger, T. A. Weber, “Computer simulation of local order in condensed phases of silicon”, Physical Review B, Vol 31, Issue 8, pp. 5262-5271, 1985.

[39] S. M. Foiles, M. I. Baskes, M. S. Daw, “Embedded-atom-method functions for the fcc metals Cu, Ag, Au, Ni, Pd, Pt, and their alloys”, Physical Review B, Vol 33, Issue 12, pp. 7983-7991, 1986.

[40] S.V. Sreenivasan, B.J. Choi, P.D. Schumaker, F. Xu, "Status of UV Imprint Lithography for Nanoscale Manufacturing," Comprehensive Nanoscience and Technology, 2011, Vol. 4, 83-116.

[41] T. Pramanik, U. Roy, L. Register, S. Banerjee, “Proposal of a Multistate Memory Using Voltage Controlled Magnetic Anisotropy of a Cross-Shaped Ferromagnet”, IEEE Transactions on Nanotechnology, Vol 14, Issue 5, Sep. 2015.

[42] J. Randall, J. Von Ehr, J. Ballard, J. Owen, R. Saini, E.Fuchs, H. Xu, S. Chen, “Atomically Precise Manufacturing: The Opportunity, Challenges, and Impact”, Atomic Scale Interconnection Machines, Springer, 2012.

[43] E. Tadmor, R. Miller, “Modeling Materials: Continuum, Atomistic and Multiscale Techniques”, Cambridge University Press, 2011

[44] https://lammps.sandia.gov/doc/Howto_couple.html

[45] A. Cherala, S.V Sreenivasan, "Molecular Dynamics Modeling Framework for Overcoming Nanoshape Retention Limits of Imprint Lithography", Microsystems and Nanotechnology, Vol 4, Article 3, Apr 2018 (https://www.nature.com/articles/s41378-018-0007-4)

[46] S.V Sreenivasan, et. al, "Nanoshape patterning techniques that allow high-speed and low-cost fabrication of nanoshape structures" US Patent No. 10,026,609, July 2018

[47] S. W. Jones, "Economic and Technical Challenges of Advanced Memory Devices", SPIE Advanced Lithography, 2019.